monitor. The scan pitch of the x and y axes was 2.5 mm, and the photon counting time per mapping point was 2.0 s. We carried out iodine mapping of non-living animals (phantoms), and iodine Kα fluorescence was produced from weakly remaining iodine elements in a rabbit skin cancer.

Keywords X-ray photon counting · Energy discrimination · X-ray camera · X-ray fluorescence · CdTe detector · DDS

1 Introduction

X-ray fluorescence (XRF) analysis [1, 2] is useful for determining the presence of various elements, and monochromatic X-rays are used to produce X-ray fluorescence. We have developed several different monochromatic X-ray generators [3–6] to produce clean K-series characteristic X-rays. In particular, plasma X-ray generators [7, 8] have major capabilities for producing extremely clean K-rays of nickel, copper, and molybdenum from weakly ionized linear plasmas consisting of metal ions and electrons. In addition, high-photon energy K-rays of tantalum and tungsten have been produced from spherical plasma targets [9, 10], and these K-rays have been applied to high-speed gadolinium K-edge angiography [9–11]. However, it is difficult to increase the X-ray duration because these flash K-rays are produced by high-energy spark discharges.

Cerium K-rays are absorbed effectively by iodine-based contrast media and are useful for performing enhanced iodine K-edge angiography. Thus, we have developed a cerium X-ray generator [12, 13], with which fine blood vessels are observed with high contrast with use of iodine media. In addition, these K-rays are usable for producing iodine fluorescence for XRF analysis.

Recently, various drug delivery systems have been developed for cancer therapy and diagnosis; the main elements in drugs are detectable by XRF analysis. In medical angiography, iodine and gadolinium contrast media are employed in computed tomographic angiography (CTA) [14] and magnetic resonance angiography (MRA) [15], respectively. These media are usable for cancer diagnosis via XRF analysis, because neocapillaries in cancers are irregular and imperfect, and weak contrast media remain for a long time in cancer regions.

In this research, we developed an XRF camera utilizing a cadmium telluride (CdTe) detector to perform preliminary experiments for XRF mapping utilizing iodine-based contrast media.

2 Experimental methods

2.1 XRF camera

Figure 1 is a block diagram of a photon-energy discriminating X-ray camera for XRF analysis (Fig. 2). The camera system consists of an x–y stage driven by a two-stage controller, a CdTe detector (Amptek, XR-100T) with an amplifier unit, a multichannel analyzer (MCA) (γPGT, MCA 4000, 4096 channels), a counter card (CC) (Contec, CNT32-4MT, Card Bus), a personal computer (PC), and a cerium X-ray generator. In this camera, objects are exposed by an X-ray beam formed by use of a 3.0-mm-diameter lead hole. Next, cerium K-series characteristic X-rays are absorbed effectively by iodine-based contrast media in

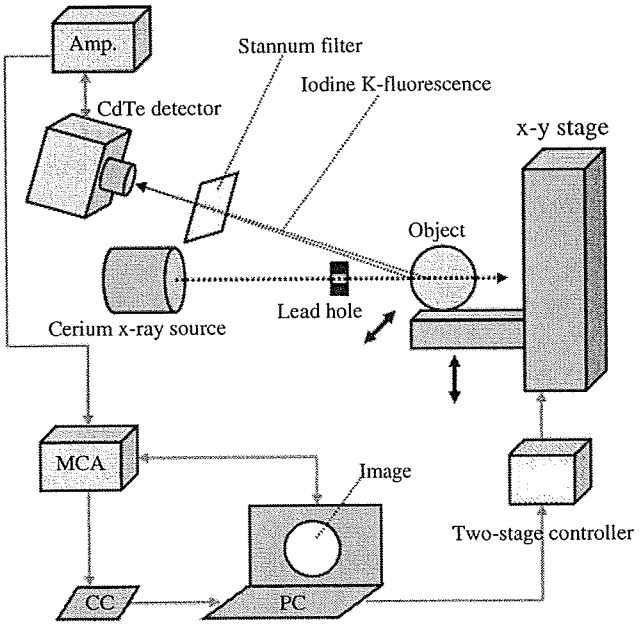

Fig. 1 Block diagram of an XRF camera utilizing a cerium X-ray generator for mapping of iodine media, where *MCA* is the multichannel analyzer, *CC* is the counter card, and *PC* is the personal computer

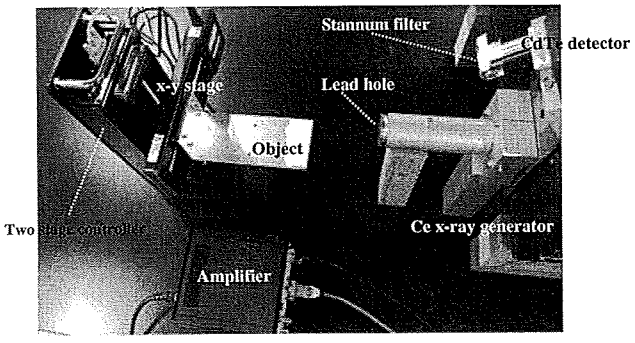

Fig. 2 Experimental setup of the XRF camera

objects, and iodine fluorescence is produced from the objects. Iodine Kα rays are selected out with a 58-μm-thick stannum filter and are detected by the CdTe detector. The X-ray photons with energies from 27 to 30 keV (Kα rays) are discriminated out by the MCA, and their counting signals from the MCA are sent to the CC. The objects are moved and scanned by the x–y stage in conjunction with the controller, and X-ray images obtained by iodine mapping are shown on the PC monitor.

The X-ray mapping was carried out by repetition of the static counting and the moving of an object. The moving velocity was 5.0 mm/s. With this camera, the total scanning time T is equal to the X-ray exposure time for mapping, and T is given by

$$T = (t_c + t_m)\, xy/S_x S_y, \tag{1}$$

where t_c is the photon counting time per mapping point, t_m is the moving time between two points, x is the horizontal dimension of the scanning field, y is the vertical dimension, and s_x and s_y are moving steps in the horizontal and vertical directions, respectively. Although the maximum scan-field dimensions are 100 mm × 100 mm, the dimensions were reduced to 50 mm × 50 mm for decreasing T. In this experiment, x, y, s_x, s_y, t_c, and t_m are 50 mm, 50 mm, 2.5 mm, 2.5 mm, 2.0 s, and 0.5 s, respectively, and T is calculated as 1,000 s.

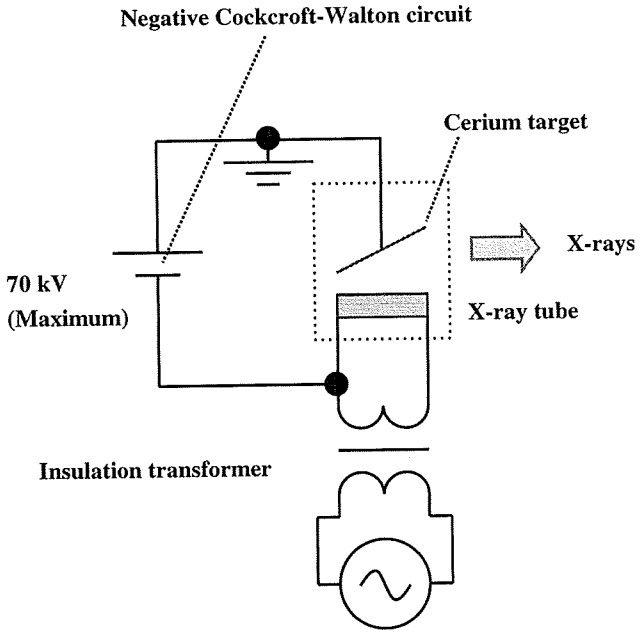

Fig. 3 Main circuit of the cerium X-ray generator

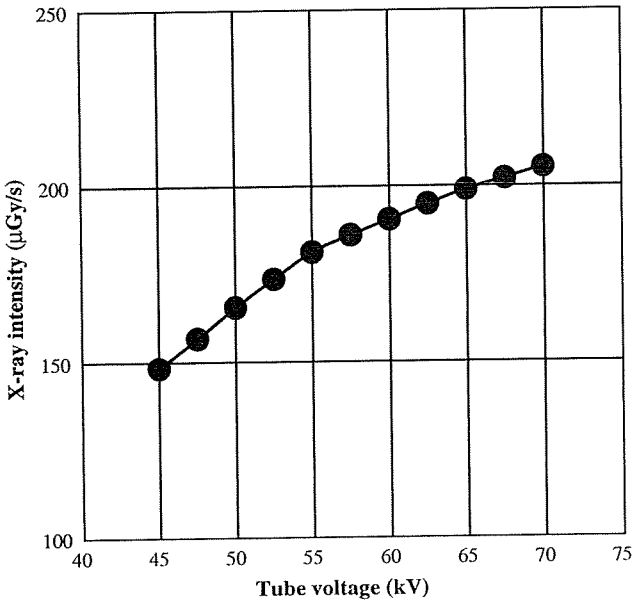

Fig. 4 X-ray intensities without a stannum filter at 1.0 m from the X-ray source according to changes in tube voltage at a tube current of 0.4 mA

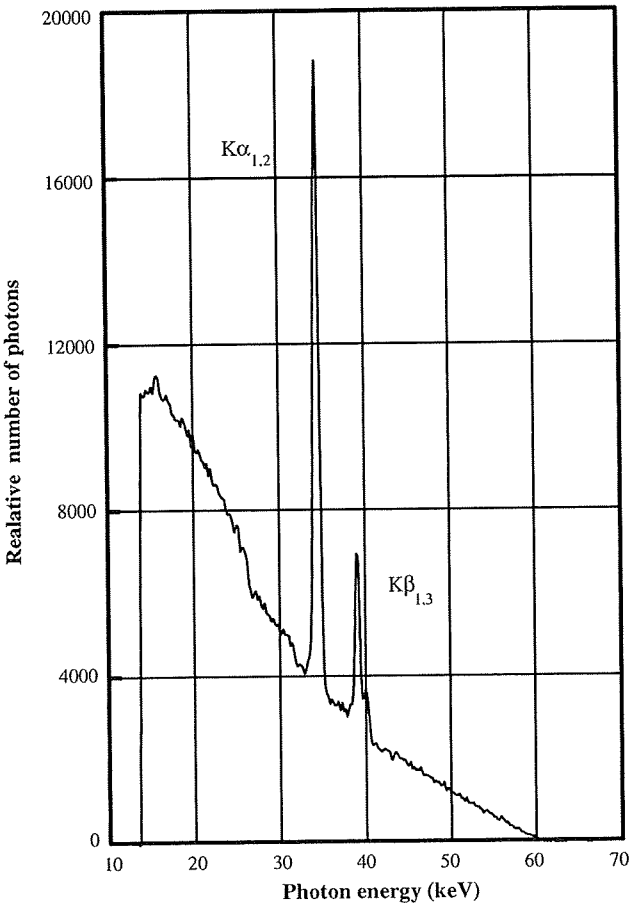

Fig. 5 X-ray spectra without a stannum filter from a cerium target at a tube voltage of 60 kV

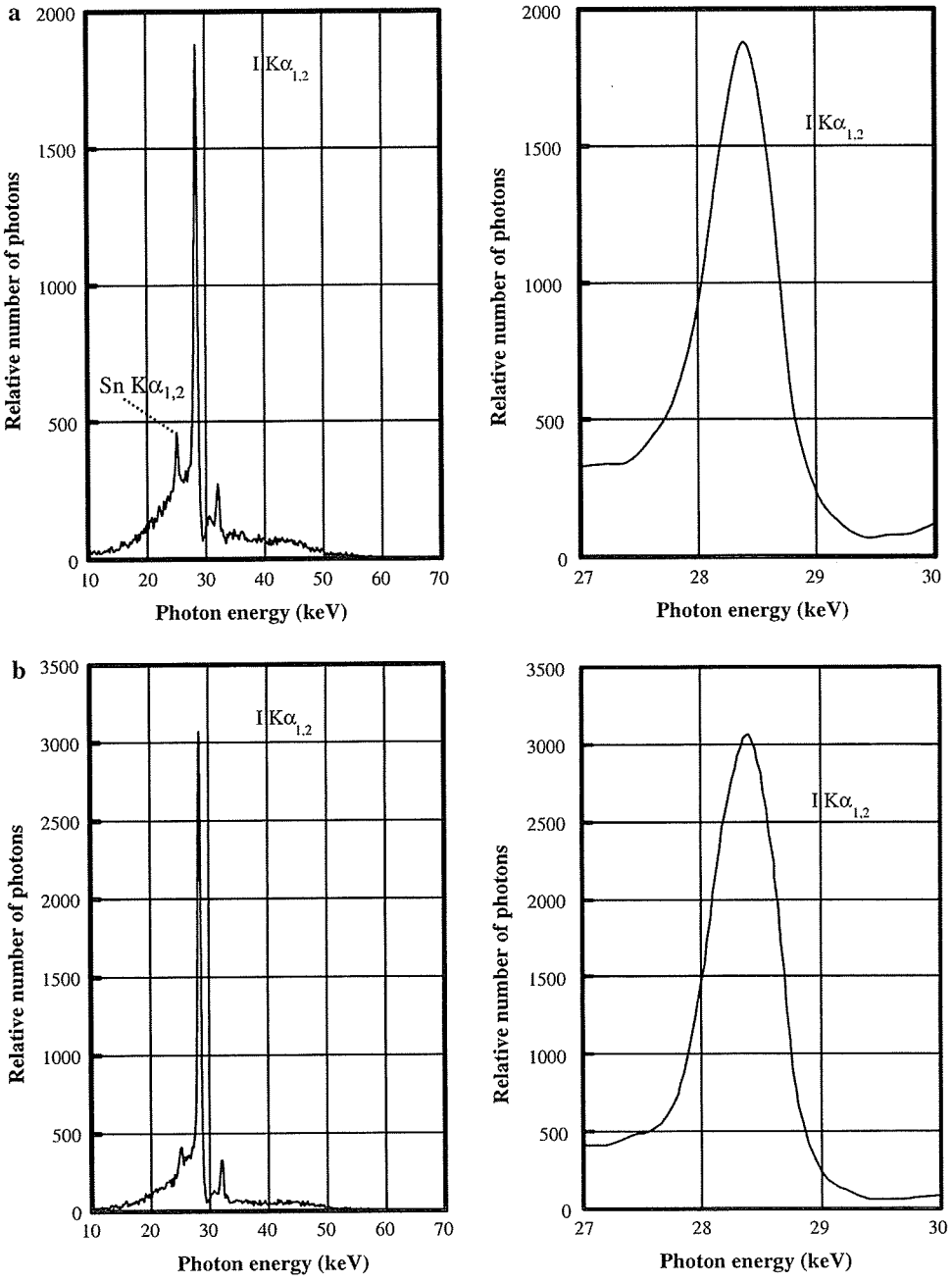

Fig. 6 X-ray spectra with a 58-µm-thick stannum filter from glass vials filled with two iodine media with densities of **a** 15 mg/ml and **b** 30 mg/ml (*right side* selected iodine $K\alpha_{1,2}$ rays)

2.2 Cerium X-ray generator

The cerium X-ray generator consists of a main controller and an X-ray tube unit with a Cockcroft-Walton circuit and a cerium target tube (Hitachi Medical, Ce-sp70 k) for enhanced K-edge angiography. The tube voltage, current, and exposure time can be set by the controller. The high-voltage line employs a negative Cockcroft-Walton circuit to decrease the dimensions of the tube unit. The X-ray tube is a fixed anode diode with a cerium target with an anode angle of 22°. In the X-ray tube, negative high voltages are applied to the cathode, and the anode (target) is connected to the tube unit case (ground potential) to cool the anode and the target effectively (Fig. 3). In this experiment, the tube voltage ranged from 45 to 65 kV, and the tube current was 0.40 mA (maximum current).

3 Results

3.1 X-ray intensity and spectra

The X-ray intensity without a stannum filter was measured using an ionization chamber (Victoreen, 660) with a 400-

cm^3-volume probe (660-5) at 1.0 m from the X-ray source and a tube current of 0.40 mA (Fig. 4). When the tube voltage was increased, the X-ray intensity increased. At a tube voltage of 60 kV, the X-ray intensity was 190 μGy/s.

To measure X-ray spectra without a stannum filter at photon energies ranging from 14 to 70 keV, we employed a CdTe detector (Fig. 5). At a tube voltage of 60 kV, cerium K-series X-rays were detected, and the bremsstrahlung X-ray intensity increased with decreasing photon energy. Figure 6 shows spectra from glass vials filled with iodine media with densities of 15 and 30 mg/ml. The iodine Kα intensity increased with increasing iodine density, and

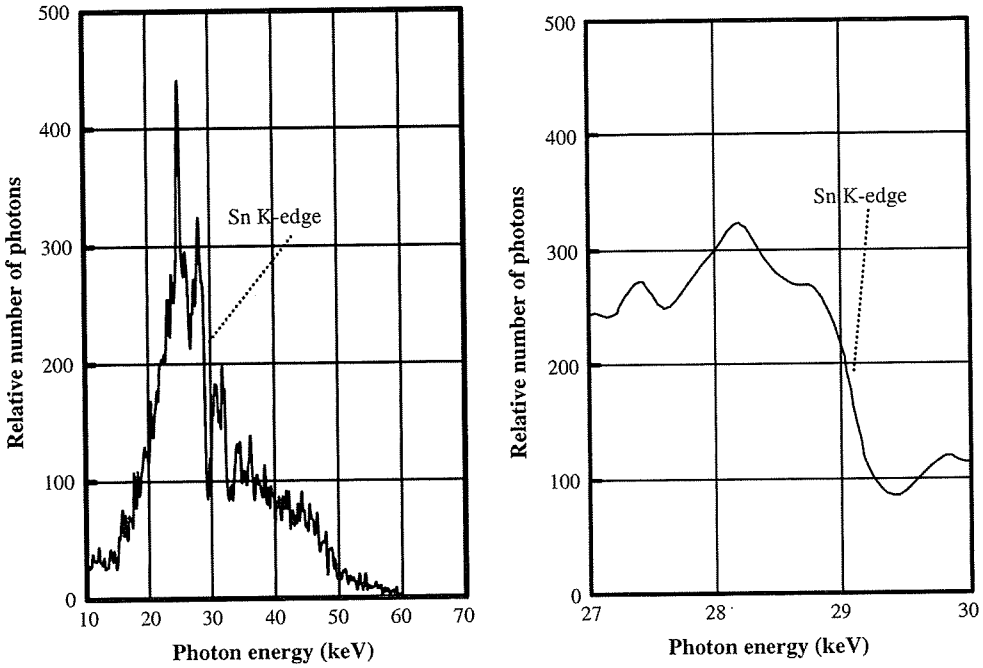

Fig. 7 X-ray spectra with a 58-μm-thick stannum filter from a glass vial filled with water at a tube voltage of 60 kV (*right side* background X-ray spectra)

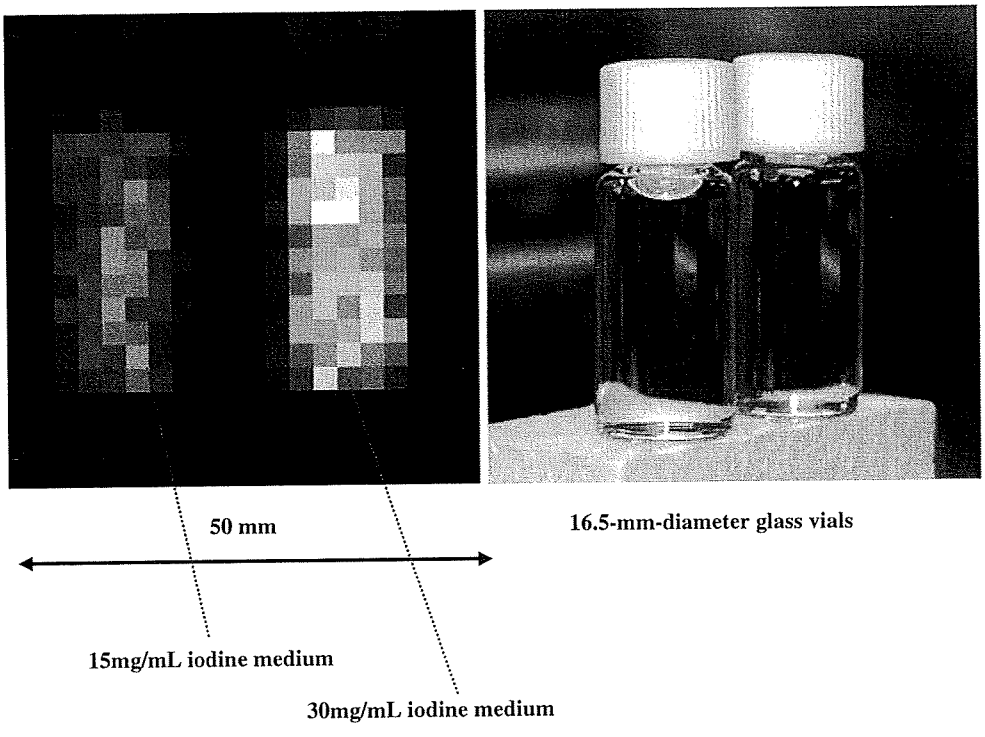

Fig. 8 X-ray image of two 16.5-mm-diameter glass vials filled with iodine media with densities of 15 and 30 mg/ml

stannum Kα fluorescence from the filter was observed. As compared with background intensities, the iodine Kα intensities were high, and we observed stannum K-edges (Fig. 7).

3.2 XRF mapping

In the XRF mapping, the maximum and minimum counts correspond to the maximum and minimum image densities,

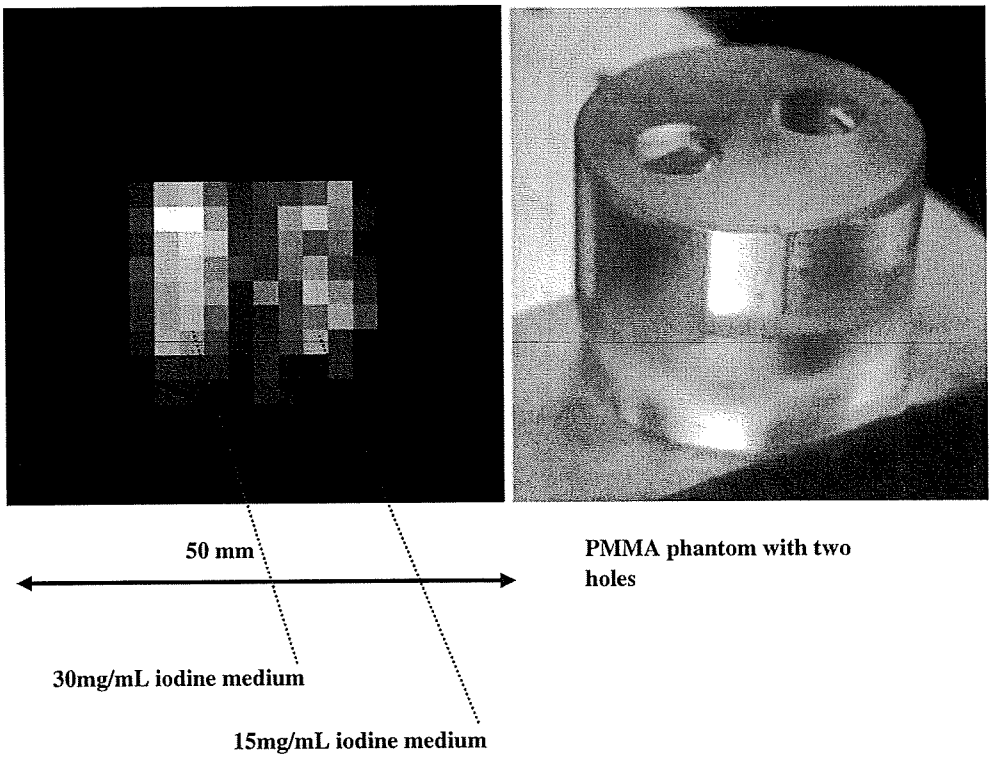

Fig. 9 X-ray image of a PMMA phantom with two 8.0-mm-diameter holes filled with iodine media with densities of 15 and 30 mg/ml

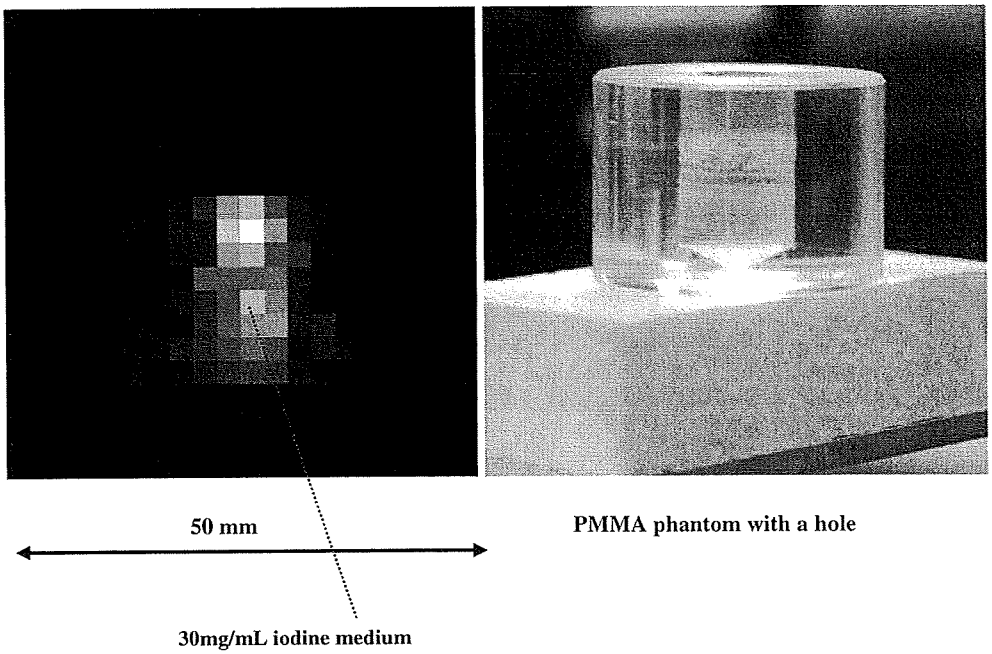

Fig. 10 X-ray image of a PMMA phantom with a 8.0-mm-diameter hole filled with iodine medium with a density of 30 mg/ml

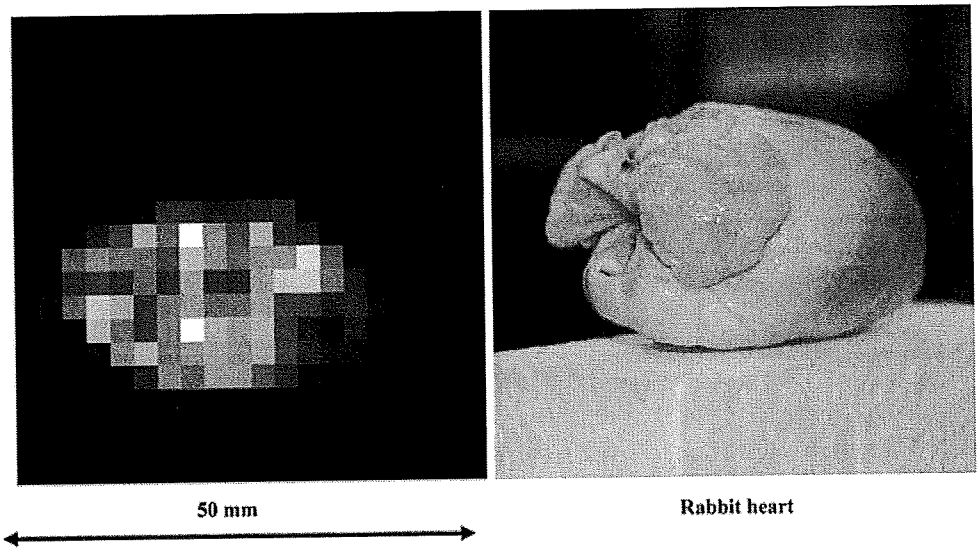

Fig. 11 X-ray image of a rabbit heart for angiography. Coronary arteries are filled with iodine microspheres

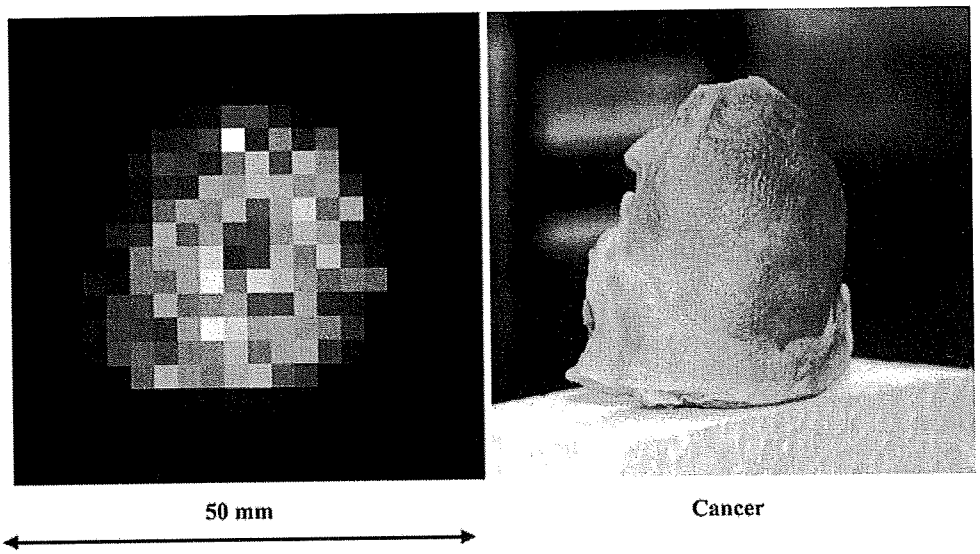

Fig. 12 X-ray image of a rabbit skin cancer. Weakly remaining iodine elements in a cancer region were detected

respectively, and the pixel sizes are equal to the steps on the x and y axes of 2.5 mm × 2.5 mm. The mapping image was constructed as a Bitmap file with the maximum and minimum densities of 255 (white) and 0 (black), respectively. Figure 8 shows an X-ray image of two 16.5-mm-diameter glass vials filled with two different-density contrast media of 15 and 30 mg/ml. The image density decreases with decreasing iodine density. When we used a polymethyl methacrylate (PMMA) phantom with two holes of 8.0 mm in diameter, two different-density media were observed (Fig. 9). Figure 10 shows an image of a PMMA phantom with an 8.0-mm-diameter hole filled with iodine medium at a density of 30 mg/ml. In both PMMA phantoms, scattering X-rays with energies beyond the iodine K-edge produce iodine fluorescence in the iodine medium, and the fluorescence is detected by the CdTe detector. Thus, the hole dimensions increased slightly by approximately 1 pixel (2.5 mm).

An image of an extracted rabbit heart for angiography is shown in Fig. 11. Coronary arteries were filled with iodine microspheres 15 μm in diameter, and iodine elements in blood vessels were detected by mapping. In mapping of a rabbit skin cancer, iodine elements that remained in the cancer were detected (Fig. 12).

4 Discussion

We developed an XRF camera utilizing a cerium X-ray generator and detected iodine Kα rays from objects with a photon energy resolution of 1.5 keV. The count rate of the Kα rays increased with increasing iodine density, and

iodine fluorescence was detected from a cancerous region in a rabbit ear. With PMMA phantoms, because Kα fluorescence is produced by the scattering beam from the PMMA regions, these photons should be subtracted from the mapping counts.

The spatial resolution improved with decreasing sampling pitches on the x and y axes and with decreasing beam diameter for scanning. At a constant tube voltage of 60 kV, the sampling time decreased with increasing count rate of iodine Kα rays by increasing the iodine density at a maximum tube current of 0.4 mA.

Recently, an energy-discriminating 64-channel CdTe linear detector, developed by Hamamatsu Photonics, has been useful for constructing an X-ray camera with a stage. As compared with the single detector described in this paper, the X-ray exposure time can be decreased when the linear detector is used. However, it is not easy to determine the photon energy just beyond the iodine K-edge of 33.2 keV and to control the energy width.

For increasing the count rate of a CdTe detector setup, the time constants in the amplifier circuits should be minimized so that pileups of event signals without a decrease in energy resolution are prevented. In conjunction with a multipixel photon counter, a high-light-yield scintillator with a short decay time (below 1 ns) is usable for discriminating photon energy, and a high-speed X-ray photon-discriminating system for decreasing the total scanning time for imaging will become possible.

Acknowledgments This work was supported by Grants-in-Aid for Scientific Research and Advanced Medical Scientific Research from MECSST, Health and Labor Sciences Research Grants, Grants from the Keiryo Research Foundation, Promotion and Mutual Aid Corporation for Private Schools of Japan, the Japan Science and Technology Agency, and the New Energy and Industrial Technology Development Organization.

References

1. Takahashi Y, Yamamoto K, Ohshima K, Yukino K, Okamura FP. X-ray fluorescence analysis of rare-earth atoms in materials by use of ultrashort wavelength X-rays. Jpn J Appl Phys. 1998; 37:L556–8.
2. Liu Z, Kawamura J, Nagasono M, Maeda K, Kawai J. Determination of the structure of boron subphosphide by P Kβ X-ray fluorescence spectra. J Electron Spectrosc Relat Phenom. 2004; 135:73–81.
3. Sato E, Sagae M, Tanaka E, Hayasi Y, Germer R, Mori H, et al. Quasi-monochromatic flash X-ray generator utilizing a disk-cathode molybdenum tube. Jpn J Appl Phys. 2004;43:7324–8.
4. Sato E, Tanaka E, Mori H, Kawai T, Inoue T, Ogawa A, et al. Characteristic X-ray generator utilizing angle dependence of bremsstrahlung X-ray distribution. Jpn J Appl Phys. 2006; 45:2845–9.
5. Sato E, Sugiyama H, Ando M, Tanaka E, Mori H, Kawai T, et al. Tunable narrow-photon-energy X-ray generator utilizing a tungsten-target tube. Rad Phys Chem. 2006;75:2008–13.
6. Sato E, Tanaka E, Mori H, Kawai T, Inoue T, Ogawa A, et al. Tunable narrow-photon-energy x-ray source using a silicon single crystal. SPIE. 2007;6706:670610-1-7.
7. Sato E, Tanaka E, Mori H, Kawai T, Sato S, Takayama K. Clean monochromatic X-ray irradiation from weakly ionized linear copper plasma. Opt Eng. 2005;44: 049002-1-6.
8. Sato E, Hayasi Y, Germer R, Tanaka E, Mori H, Kawai T, et al. X-ray spectra from weakly ionized linear copper plasma. Jpn J Appl Phys. 2006;45:5301–6.
9. Sato E, Hayasi Y, Kimura K, Tanaka E, Mori H, Kawai T, et al. Enhanced K-edge angiography utilizing tantalum plasma X-ray generator in conjunction with gadolium-based contrast media. Jpn J Appl Phys. 2005;44:8716–21.
10. Sato E, Hayasi Y, Tanaka E, Mori H, Kawai T, Inoue T, et al. K-edge angiography utilizing a tungsten plasma X-ray generator in conjunction with gadolinium-based contrast media. Rad Phys Chem. 2006;75:1841–9.
11. Sato Y, Sato E, Ehara S, Enomoto T, Tanaka E, Mori H, et al. Magnification K-edge angiography utilizing 100 μm-focus tungsten tube and gadolinium-based contrast media. Jpn J Appl Phys. 2008;47:4772–6.
12. Sato E, Tanaka E, Mori H, Kawai T, Ichimaru T, Sato S, et al. Demonstration of enhanced K-edge angiography using a cerium target X-ray generator. Med Phys. 2004;31:3017–21.
13. Sato E, Tanaka E, Mori H, Kawai T, Inoue T, Ogawa A, et al. Variations in cerium X-ray spectra and enhanced K-edge angiography. Jpn J Appl Phys. 2005;44:8204–9.
14. Herzog C, Dogan S, Diebold T, Khan MF, Ackermann H, Schaller S, et al. Multi-detector row CT versus coronary angiography: preoperative evaluation before totally endoscopic coronary artery bypass grafting. Radiology. 2003;229:200–8.
15. Hernandez RJ, Strouse PJ, Londy FJ, Wakefield TW. Gadolinium-enhanced MR angiography (Gd-MRA) of thoracic vasculature in an animal model using double-dose gadolinium and quiet breathing. Pediatr Radiol. 2001;31:589–93.

Radiol Phys Technol (2009) 2:77–86
DOI 10.1007/s12194-008-0048-8

Embossed radiography utilizing energy subtraction

Akihiro Osawa · Manabu Watanabe · Eiichi Sato · Hiroshi Matsukiyo · Toshiyuki Enomoto · Jiro Nagao · Purkhet Abderyim · Katsuo Aizawa · Etsuro Tanaka · Hidezo Mori · Toshiaki Kawai · Shigeru Ehara · Shigehiro Sato · Akira Ogawa · Jun Onagawa

Received: 31 July 2008 / Revised: 17 November 2008 / Accepted: 18 November 2008 / Published online: 18 December 2008
© Japanese Society of Radiological Technology and Japan Society of Medical Physics 2008

Abstract Currently, it is difficult to carry out refraction-contrast radiography by using a conventional X-ray generator. Thus, we developed an embossed radiography system utilizing dual-energy subtraction for decreasing the absorption contrast in unnecessary regions, and the contrast resolution of a target region was increased by use of image-shifting subtraction and a linear-contrast system in a flat panel detector (FPD). The X-ray generator had a 100-μm-focus tube. Energy subtraction was performed at tube voltages of 45 and 65 kV, a tube current of 0.50 mA, and an X-ray exposure time of 5.0 s. A 1.0-mm-thick aluminum filter was used for absorbing low-photon-energy bremsstrahlung X-rays. Embossed radiography was achieved with cohesion imaging by use of the FPD with pixel sizes of 48 × 48 μm, and the shifting dimension of an object in the horizontal direction ranged from 100 to 200 μm. At a shifting distance of 100 μm, the spatial resolutions in the horizontal and vertical directions measured with a lead test chart were both 83 μm. In embossed radiography of non-living animals, we obtained high-contrast embossed images

A. Osawa (✉) · M. Watanabe · H. Matsukiyo · T. Enomoto · J. Nagao
The 3rd Department of Surgery, Toho University School of Medicine, 2-17-6 Ohashi, Meguro-ku, Tokyo 153-8515, Japan
e-mail: a.osawa@indigo.plala.or.jp

E. Sato
Department of Physics, Iwate Medical University, 2-1-1 Nishitokuta, Yahaba 028-3694, Japan

P. Abderyim
Department of Computer and Information Sciences, Faculty of Engineering, Iwate University, 4-3-5 Ueda, Morioka 020-8551, Japan

K. Aizawa
Tokyo Medical University, 6-1-1 Shinjyuku, Shinjyuku-ku, Tokyo 160-8402, Japan

E. Tanaka
Department of Nutritional Science, Faculty of Applied Bio-science, Tokyo University of Agriculture, 1-1-1 Sakuragaoka, Setagaya-ku, Tokyo 156-8502, Japan

H. Mori
Department of Cardiac Physiology, National Cardiovascular Center Research Institute, 5-7-1 Fujishirodai, Suita, Osaka 565-8565, Japan

T. Kawai
Electron Tube Division #2, Hamamatsu Photonics K.K, 314-5 Shimokanzo, Iwata, Shizuoka 438-0193, Japan

S. Ehara
Department of Radiology, School of Medicine, Iwate Medical University, 19-1 Uchimaru, Morioka 020-8505, Japan

S. Sato
Department of Microbiology, School of Medicine, Iwate Medical University, 19-1 Uchimaru, Morioka 020-8505, Japan

A. Ogawa
Department of Neurosurgery, School of Medicine, Iwate Medical University, 19-1 Uchimaru, Morioka 020-8505, Japan

J. Onagawa
Department of Electronics, Faculty of Engineering, Tohoku Gakuin University, 1-13-1 Chuo, Tagajo, Miyagi 985-8537, Japan

of fine bones, gadolinium oxide particles in the kidney, and coronary arteries approximately 100 μm in diameter.

Keywords Embossed radiography · Digital subtraction · Energy subtraction · Contrast resolution · Polychromatic X-rays

1 Introduction

Extremely clean monochromatic parallel X-ray beams have been formed by use of synchrotrons and single silicon crystals, and these beams have been applied to carrying out enhanced iodine K-edge angiography [1–3], phase-contrast radiography [4–6], and topography [7, 8]. For performing K-edge angiography, monochromatic X-rays with energies just beyond the iodine K-edge of 33.2 keV have been used, because these rays are absorbed effectively by iodine-based contrast media. Currently, phase-contrast radiography is based primarily on X-ray refraction in objects, and soft tissues, such as breast cancers [6], can be imaged with high contrast. However, it is difficult to carry out phase-contrast imaging of contrast media for medical angiography, delivered nano-particles, and hard tissues. Two-dimensional X-ray topography also is a method for imaging defects in crystals by utilizing X-ray diffraction.

Without the use of synchrotrons, several different monochromatic X-ray sources [9–12] have been developed, and K-edge angiography, phase radiography, and topography have been carried out. In particular, a cerium X-ray generator [13, 14] has been developed and has been applied to carrying out cone-beam K-edge angiography because cerium Kα rays (34.6 keV) are absorbed effectively by iodine media. Next, phase radiography for edge enhancement of objects has been performed by magnification radiography with a microfocus X-ray generator and polychromatic X-rays [15]. However, this conventional phase radiography is usable for imaging only of soft tissues, and a microfocus X-ray tube is necessary. Therefore, we are very interested in the development of a novel radiography system instead of the phase imaging by use of a generalized digital X-ray image sensor and a conventional large-focus tungsten tube that produces polychromatic X-rays.

Energy subtraction radiography [16, 17] is an important technique for imaging target regions in vivo by removing muscle and bone regions from radiograms. Currently, two different energy radiograms are obtained with two different tube voltages, and dual-energy subtraction radiography is carried out by digital subtraction between the high- and low-energy images. Furthermore, embossed radiography (ER) [18] is a novel technique for constructing concavo-convex radiography, such as phase-differential imaging, and is realizable with digital image subtraction after image shifting with an optimal dimension between two images. The image shifting is carried out by moving an X-ray source [18], by moving an object precisely, and by shifting image pixels in a flat panel detector (FPD) with use of a computer program before subtraction. By use of this radiography, the target region in various objects can be imaged with embossing, and the maximum contrast resolution is achieved without a drop in spatial resolution. In addition, our ultimate goal of embossing is the development of a novel computed tomography (CT) system with a high contrast resolution for cancer diagnosis that utilizes a drug delivery system.

In our research, major objectives are as follows: construction of edge enhancement radiography such as phase-differential imaging utilizing embossing, an increase in the contrast resolution of the target region, and energy subtractions of contrast media and nano-particles. Therefore, we carried out preliminary experiments for ER utilizing two-shot dual-energy subtraction by shifting objects.

2 Experimental methods

2.1 Experimental setup for ER

Figure 1 shows an experimental setup for performing ER utilizing an FPD (1024EV, Rad-icon Imaging, Santa Clara, CA). This experiment is carried out for a fundamental study on single-dimensional ER, although two-dimensional shifting is realizable with a pixel-shifting computer program. ER was performed by digital subtraction, cohesion radiography, and shifting of an object with a dimension ranging from 100 to 200 μm and with a traveling microscope (NRM–2XZ, Shimadzu Rika, Tokyo, Japan) that had a length resolution of 10 μm. The computer program names for observing raw-file images and for carrying out

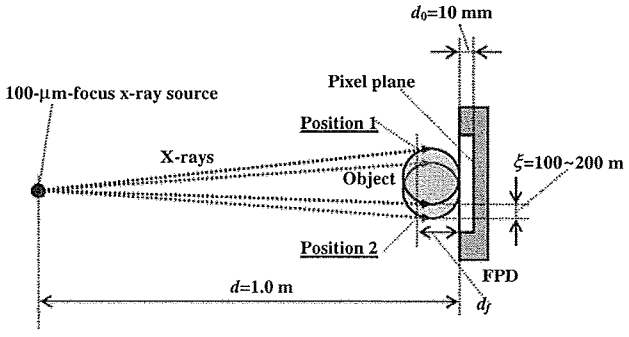

Fig. 1 Experimental setup for performing embossed radiography (ER) utilizing energy subtraction, where ξ is the image-shifting dimension in the FPD, d_f is the distance from the FPD to the position in the object, d_0 is the distance between the FPD face and the pixel plane, and d is the distance between the source and the FPD face

subtraction radiography were ShadoCam (Rad-icon Imaging, Santa Clara, CA) and EnergyCalc Composition 1.0 (AD Science, Funabashi, Japan), respectively.

For carrying out ER such as phase-differential imaging, the minimum shifting dimension is two times the pixel size of 48 μm, and the maximum shifting dimension is almost equal to an allowable spatial resolution. Absorption contrast of unnecessary regions is decreased by energy subtraction. An object is exposed by an X-ray generator with a 100-μm-focus X-ray tube, and the first radiogram is obtained at position 1 in Fig. 1. The second radiogram is taken at position 2 in Fig. 1 after shifting of the object. Two radiograms are taken using two different photon energy spectra with maximum photon energies of 45 and 65 keV, and are recorded as raw files. In this setup, the image shifting dimension ξ in the FPD is given by

$$\xi = \sigma(d + d_0)/(d - d_f) \cong \sigma, \tag{1}$$

where σ is the shifting dimension of the object, d_f is the distance from the FPD to the position in the object, d_0 (=10 mm) is the distance between the FPD face and the pixel plane, and d is the distance between the source and the FPD face. In our research, σ and d were determined to be 100–200 μm and 1.0 m, respectively. In dual-energy subtraction for embossing, an embossed raw-file $R_e(x, y)$ as a function of horizontal x and vertical y distances in the FPD is calculated by

$$R_e(x, y) = R_1(x, y) - KR_2(x - \xi, y), \tag{2}$$

where $R_1(x, y)$ is the first raw-file image at position 1, $R_2(x - \xi, y)$ is the second raw-file image with different energy spectra at position 2 after shifting of the object, K ($0 < K \leq 1.0$) is a constant for subtraction, and K varies by 0.1 increments.

Typical one-dimensional projection curves for ER are shown in Fig. 2. $R_1(x)$ is the first projection curve from the FPD, $KR_2(x - \xi)$ is the shifted curve for subtraction, and $R_e(x)$ is the embossed projection curve in the raw file system. In this experiment, an embossed projection curve $T(x)$ and its inverted curve $T_i(x)$ in the TIFF file system are written as

$$T(x) = \{R_1(x) - KR_2(x - \xi) - R_{\min}\} \times D_m/(R_{\max} - R_{\min}), \tag{3}$$

$$T_i(x) = D_m - T(x), \tag{4}$$

where D_m (= 255) is the maximum density, and $R_{\max}$ and $R_{\min}$ are the maximum and minimum densities of $R_e(x)$, respectively. In the FPD, the densities of 0 and D_m correspond to black and white, respectively. Therefore, the contrast resolution increases to 1 after subtraction by a linear-contrast system. The matrix size is about 1 M (1,048 × 1,048) pixels, and the pixel sizes are

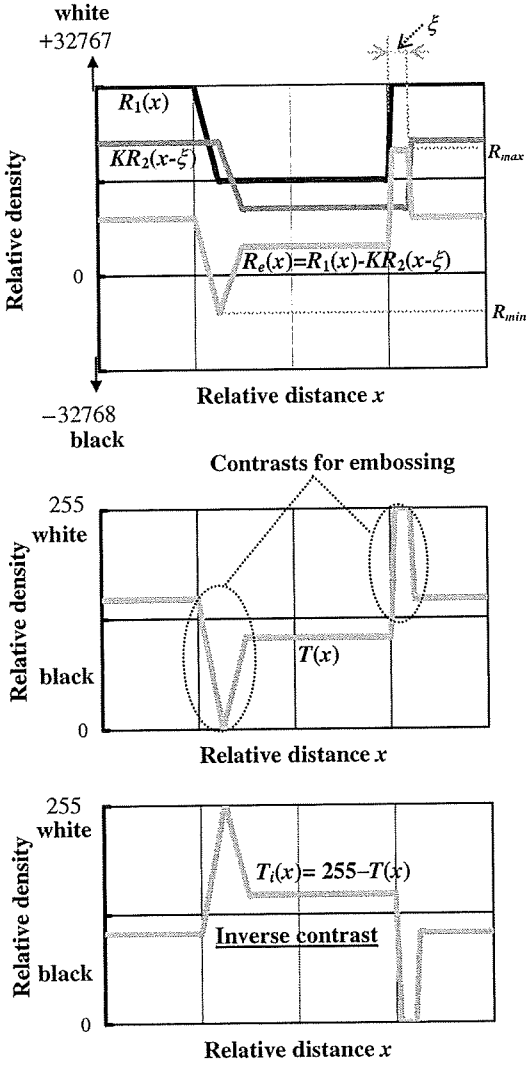

Fig. 2 One-dimensional projection curves for performing ER utilizing subtraction, where ξ the image shifting dimension in the FPD, $R_e(x)$ is the embossed projection curve in the raw file system, $R_1(x)$ is the first projection curve from the FPD, $KR_2(x - \xi)$ is the shifted curve for subtraction, K is a constant, $T(x)$ is an embossed projection curve in the TIFF file system, $T_i(x)$ is its inverted curve, and $R_{\max}$ and $R_{\min}$ are the maximum and minimum densities of $R_e(x)$, respectively

48 μm × 48 μm. The gray scale ranges from 0 to 255, and the relation between the X-ray intensity and the gray level is linear.

2.2 X-ray generator

Figure 3 shows the circuit diagram of an X-ray generator that was designed for regulating the focal size of an X-ray tube (Toshiba, 1–311) by controlling the negative bias voltage of the focusing electrode. In this experiment, the size was regulated as 100 μm at a bias voltage of −20 V because the size decreased with increasing negative bias

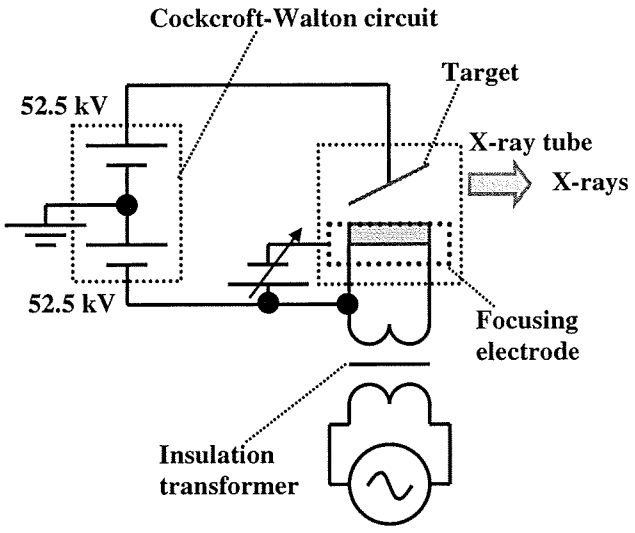

Fig. 3 Circuit diagram of a 100-μm-focus X-ray generator

voltage, and tube voltage, current, and exposure time could be controlled by a main controller. The high-voltage line employs the Cockcroft-Walton circuit, and positive and negative high voltages are applied to the anode and cathode electrodes, respectively. The filament heating current is supplied by an AC power supply with an insulation transformer that is used for isolation from the high voltage from the Cockcroft–Walton circuit. For measurement of X-ray intensity, the tube voltage ranged from 40 to 70 kV, and the tube current was regulated to be 0.50 mA. Because the maximum exposure time of the FPD was 6.0 s, the time was set as 5.0 s, which increased the X-ray intensity for radiography.

2.3 Measurement of X-ray intensity

The measurement of X-ray intensity for ER is important because the intensity is decreased by the subtraction. The X-ray intensity was measured with an ionization chamber (660, Victoreen, Solon, OH) with a 400-cm^3 volume probe (660-5, Victoreen, Solon, OH) with a tube current of 0.50 mA at 1.0 m from the X-ray source. For performing ER utilizing dual-energy subtraction, the total X-ray intensity of the two shots is equal to the exposed dose I_{ex} for patients. Thus, I_{ex} and the X-ray intensity after the subtraction I_s are given by

$$I_{ex} = I_1 + I_2, \tag{5}$$

$$I_s = I_1 - KI_2, \tag{6}$$

where I_1 and I_2 are the X-ray intensities at positions 1 and 2, respectively. Roughly speaking, the absorption contrast decreases when I_s decreases. Moreover, the image contrast reverses in a case where I_s is a negative value.

2.4 Measurement of X-ray spectra

The image contrast varies corresponding to the X-ray spectra for radiography, and we have to measure the spectral distributions before energy subtraction. In order to measure X-ray spectra, we employed a cadmium telluride (CdTe) detector (XR-100T, Amptek, Bedford, MA) and measured spectra at 1.0 m from the X-ray source. The cooled detector unit with a charge amplifier was set at 1.0 m from the X-ray source, and event signals from the detector unit were amplified again by a shaping amplifier unit. A 0.1-mm-diameter lead pinhole was set in front of the detector facing the X-ray source to decrease the photon count rate. The photon energy was discriminated by a multichannel analyzer (MCA-8000A, Amptek, Bedford, MA), and the X-ray spectra were observed on a personal computer monitor. Measurement results for the X-ray spectra are important for carrying out dual-energy subtraction because the spectral distribution is the X-ray intensity as a function of the photon energy. In particular, when we perform K-edge subtraction, we have to confirm the spectra with energies below and beyond the K-edge energy, and the spectra should be controlled to optimal distributions by selection of the tube voltage, the element of the filter, and its filter thickness.

2.5 Method for ER utilizing single-energy subtraction

Although unnecessary regions are not deleted by single-energy subtraction, we carried out single-energy ER to observe the effect of embossing. Two radiograms were taken at positions 1 and 2 at a tube voltage of 45 kV by use of the filter, and the embossing was performed by image shifting. The embossed raw-file radiogram $R_e(x, y)$ was calculated by

$$R_e(x,y) = R_{45}(x,y) - KR_{45}(x-\xi,y), \tag{7}$$

where $R_{45}(x, y)$ is a radiogram obtained with a tube voltage of 45 kV and $R_{45}(x - \xi, y)$ is a radiogram at a voltage of 45 kV after shifting of the object.

The X-ray exposure time was 5.0 s, and two embossed radiograms were obtained with K values of 1.0 and 0.7. At a K of 1.0, the absorption contrast is removed, and the embossed effect is confirmed easily. When K is decreased, the absorption contrast increases, and the embossed effect decreases. Because the absorption contrast seldom varied in a K range from 0.5 to 0.7, K was determined as 0.7 for performance of single-energy ER with absorption contrast.

2.6 Method for ER utilizing dual-energy subtraction

As compared with single-energy ER, the target regions are imaged effectively by dual-energy ER. Because the K

edges of iodine and gadolinium are 33.2 and 50.3 keV, respectively, a high-energy radiogram should be taken at an energy region beyond 50.3 keV. The minimum difference between the high and low tube voltages was approximately 20 kV. Therefore, two different energy radiograms were obtained with tube voltages of 45 and 65 kV with use of the filter, and dual-energy ER was performed by image shifting. Utilizing energy subtraction, $R_e(x,y)$ was written as

$$R_e(x,y) = R_{45}(x,y) - KR_{65}(x-\xi,y), \quad (8)$$

where $R_{65}(x - \xi, y)$ is a radiogram with a voltage of 65 kV after shifting of the object. For an increase in the embossed effect with high contrast, K is determined to be within a range from 0.7 to 1.0.

2.7 Measurement of spatial resolution

The spatial resolution of the horizontal and vertical directions was measured with a cuneal lead test chart. The resolution was measured for line pairs L per 1.0 mm. Therefore, the spatial resolution S (μm) is given by

$$S = 1,000/2L. \quad (9)$$

Thus, when five line pairs (LP) are seen, the spatial resolution is determined as 100 μm.

2.8 Making of gadolinium oxide particles

A gadolinium oxide suspension for injection was made in a high-pressure machine (Starburst Mini, Sugino Machine, Namerikawa, Japan) for dispersing micro-particles. The high-pressure dispersing was carried out five times with use of physical saline, and the average particle diameter and the density of gadolinium oxide were 700 nm and 20%, respectively.

2.9 Objects for ER

For performing ER, we used five objects as follows: a nonliving nude mouse with a weight of 15 g, a lead test chart (PTW, L659035), an extracted rabbit kidney (8 g), an extracted rabbit heart (11 g), and a dried pig vertebra (22 g). The mouse, kidney, and heart were preserved in 10% formalin solution. The kidney and heart were extracted from two different rabbits with weights of approximately 2 kg after anesthetic (5% Nembutal) injection of 1.8 ml in an ear. A renal pelvis in the kidney was filled with gadolinium oxide suspension of 0.3 ml as described above by injection, and coronary arteries were filled with iodine-based microspheres. When a 20%-microsphere suspension by use of physical saline was injected into the arteries, the saline penetrated capillaries with diameters below 10 μm and reached the veins. Thus, the 37%-iodine microspheres 15 μm in diameter remained in the arteries.

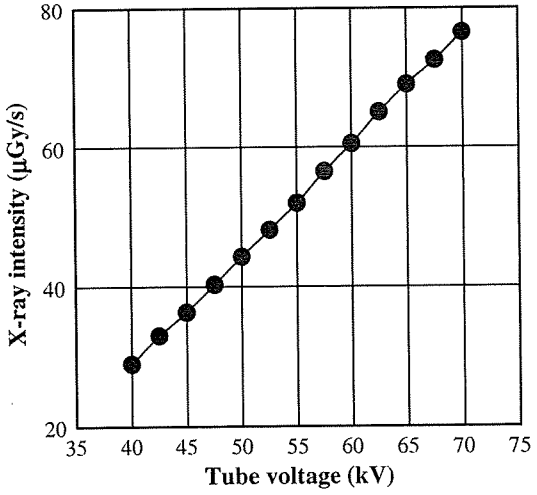

Fig. 4 X-ray intensities with a 1.0-mm-thick aluminum filter at 1.0 m from the X-ray source and a tube current of 0.5 mA

3 Results

3.1 X-ray intensity

When the tube voltage was increased, the X-ray intensity after penetrating a 1.0-mm-thick aluminum filter increased (Fig. 4). At a tube voltage 65 kV, the X-ray intensity was 69.0 μGy/s, with errors of less than 0.2%. For carrying out dual-energy ER, the exposure time was 5.0 s, and the low and high tube voltages were 45 and 65 kV, respectively. Thus, the total exposed dose for patients was approximately 0.5 mGy. In our experimental results for chest radiography with a computed radiography (CR) system, because the exposure dose ranged from 0.2 to 1.0 mGy, these values were almost equal to the dose in dual-energy ER.

3.2 X-ray spectra

When the tube voltage was increased, both the maximum photon energy and the spectral peak energy increased (Fig. 5). When the filter was used for absorbing soft bremsstrahlung rays, the peak energies at tube voltages of 45 and 65 kV were 23 and 27 keV, respectively, where the K-edge absorption of the CdTe detector was considered.

3.3 ER utilizing single-energy subtraction

Figure 6 shows ER of a nude mouse according to changes in K. As compared with normal radiography (Fig. 6a), the

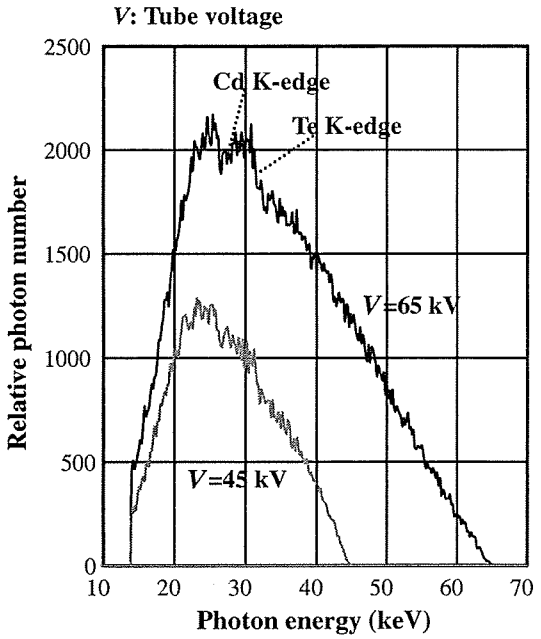

Fig. 5 X-ray spectra measured with a cadmium telluride detector and the filter at tube voltages of 45 and 65 kV

absorption contrast was removed at a K of 1.0 (Fig. 6b), and the contrast increased with decreasing K (Fig. 6c). With embossing, edge enhancement images of a mouse skull were obtained. In this single-energy ER, because the object was shifted horizontally, the vertical edges were effectively enhanced.

3.4 ER utilizing dual-energy subtraction

The spatial resolution of the horizontal and vertical directions was measured with a lead test chart (Fig. 7). In cohesion radiography, the spatial resolution of the horizontal and vertical directions was approximately 80 μm. ER was performed at a K of 0.7, and the spatial resolution fell with increasing shifting dimension in the horizontal direction. The horizontal spatial resolutions were 83 and 143 μm at the shifting dimensions of 100 and 200 μm, respectively (Fig. 7a). However, the resolution seldom varied with increasing shifting dimension, and 83-μm lines were visible in the vertical direction (Fig. 7b). Therefore, the shifting dimension should be controlled corresponding to the allowable spatial resolution, and two-dimensional image shifting is useful for enhancing of the target region.

Figure 8 shows a radiogram and an embossed radiogram of a region of the mouse abdomen. The embossed radiogram was calculated by a formula (8) with changing K. In radiography with a tube voltage of 45 kV, a mouse dung was barely visible. When K was increased in dual-energy ER, the absorption contrast of the muscle decreased

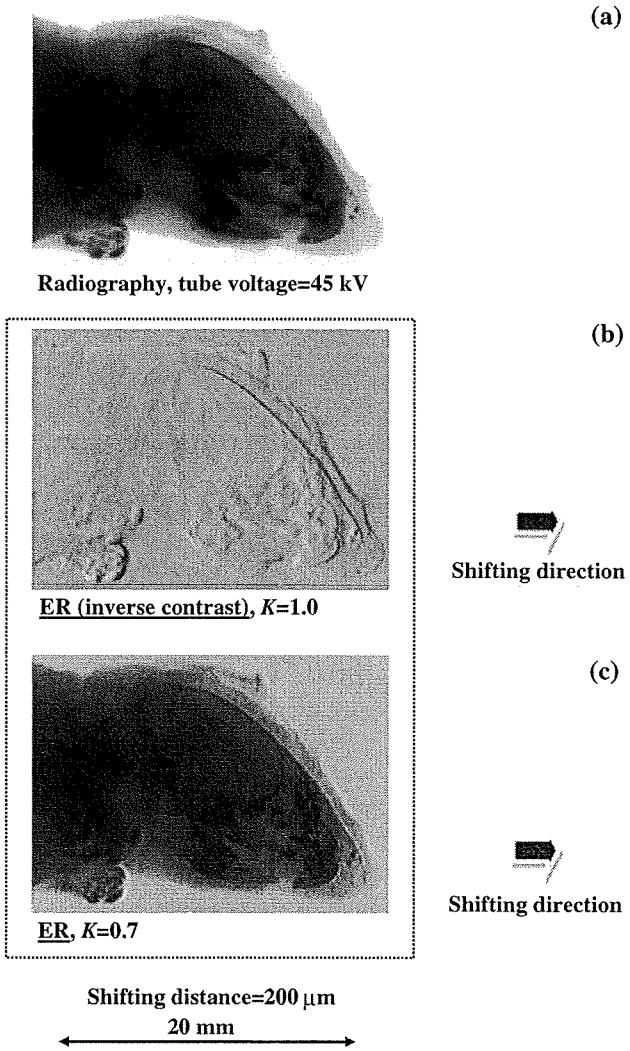

Fig. 6 Radiography of a nude-mouse head at a tube voltage of 45 kV. **a** Normal radiography, **b** embossed radiography (ER) at a K of 1.0, and **c** ER at a K of 0.7. Edge enhancement images of a skull were obtained in ER with use of single-energy subtraction

slightly, and both the dung and the dorsal were observed clearly with embossing.

Radiography of a rabbit kidney is shown in Fig. 9, and gadolinium oxide particles 700 nm in average diameter were used for observing a renal pelvis in the kidney. As compared with a normal radiogram, the image contrast of the renal pelvis was improved by use of embossing. With increasing K, the absorption contrast of the muscle decreased too, and the contrast of the renal pelvis was improved. For imaging of the pelvis, an iodine-based contrast medium used in medical angiography and a cerium oxide suspension are also usable.

Angiograms of an extracted rabbit heart with iodine-based microspheres 15 μm in diameter are shown in Fig. 10. According to increases in K with embossing, the contrast of heart muscles slightly decreased, and fine coronary arteries

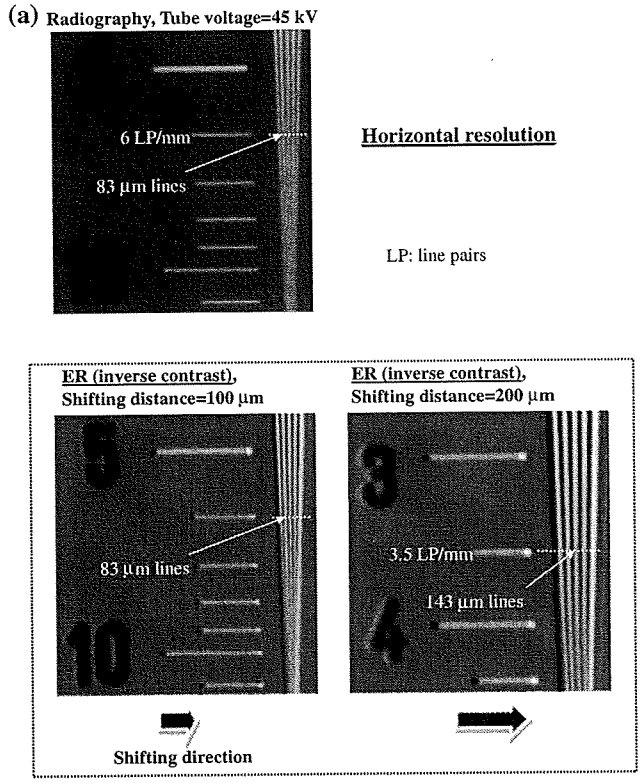

Fig. 7 Radiography and ER of a lead test chart according to changes in the shifting distance in the horizontal direction. **a** Horizontal spatial resolutions and **b** vertical spatial resolution

were clearly observed at K values ranging from 0.7 to 1.0. To observe fine blood vessels below 100 μm in diameter, the shifting dimension should be minimized to 100 μm.

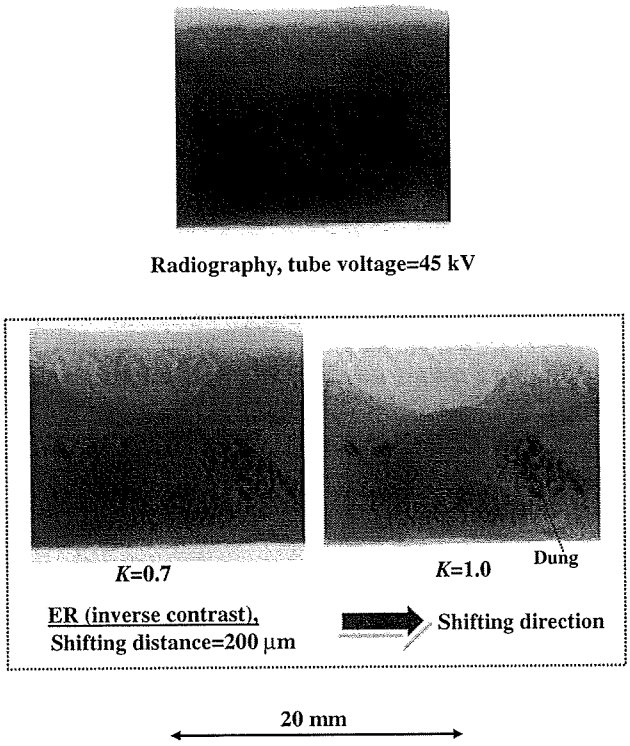

Fig. 8 Radiography of a mouse abdomen. Dung is clearly seen on ER

In radiography of a vertebra, the contrast resolution increased with embossing, and bone structures were visible (Fig. 11). In dual-energy ER for observing dry bones, because the image contrast decreased with increasing K, the single-energy ER was usable.

4 Conclusion and outlook

We performed ER by utilizing energy subtraction and image shifting. In this method of radiography, concavo-convex images were obtained by shifting of the second image, and absorption contrasts of unnecessary regions were decreased by use of energy subtraction. As compared with conventional radiography, the contrast resolution of target regions increased to approximately 1 when we used a linear-contrast system. Therefore, it was easy to observe target regions as embossed images without decreasing the spatial resolution. Currently, although spatial resolution decreases with increasing shifting distance ξ, the minimum shifting distance ξ_{min} should be kept at approximately 100 μm to enhance embossing and is written as

$$\xi_{min} \cong 2s_p \leq \xi \leq \xi_{max}, \tag{10}$$

where s_p is the pixel size of 48 μm and ξ_{max} is the maximum shifting distance corresponding to the allowable spatial resolution.

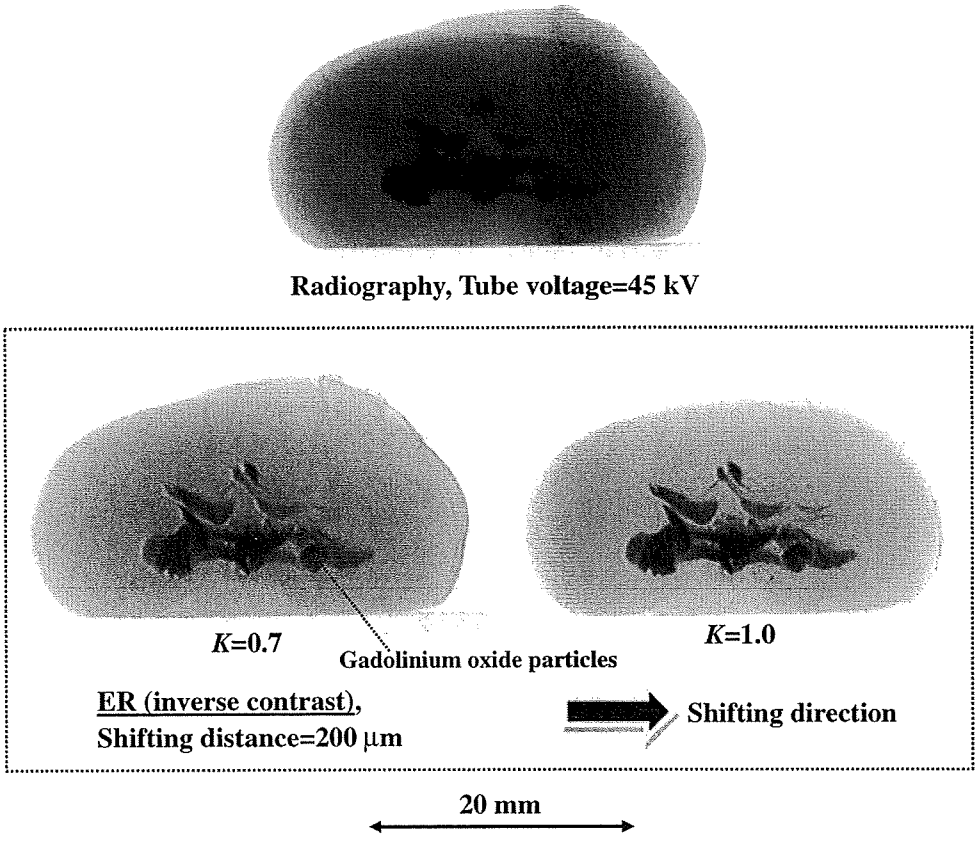

Fig. 9 Radiograms of a rabbit kidney. In ER, a renal pelvis is visible with gadolinium oxide nano-particles

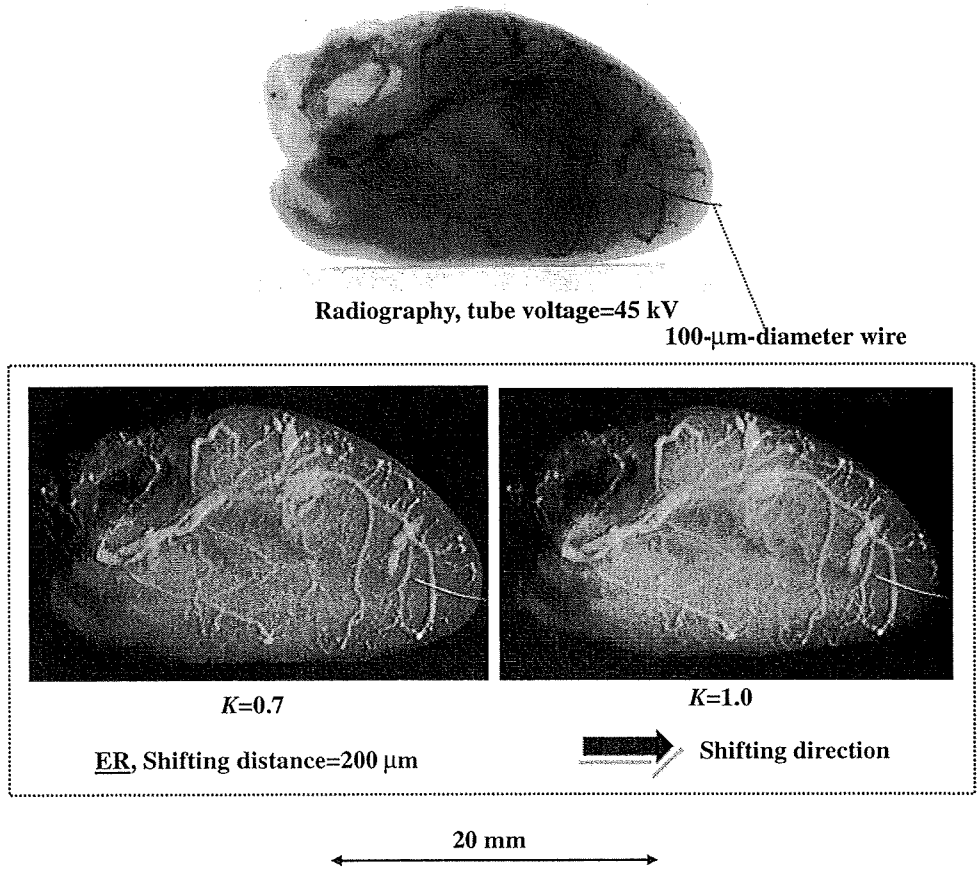

Fig. 10 Radiography of a rabbit heart using iodine-based microspheres. Coronary arteries are clearly observed in ER

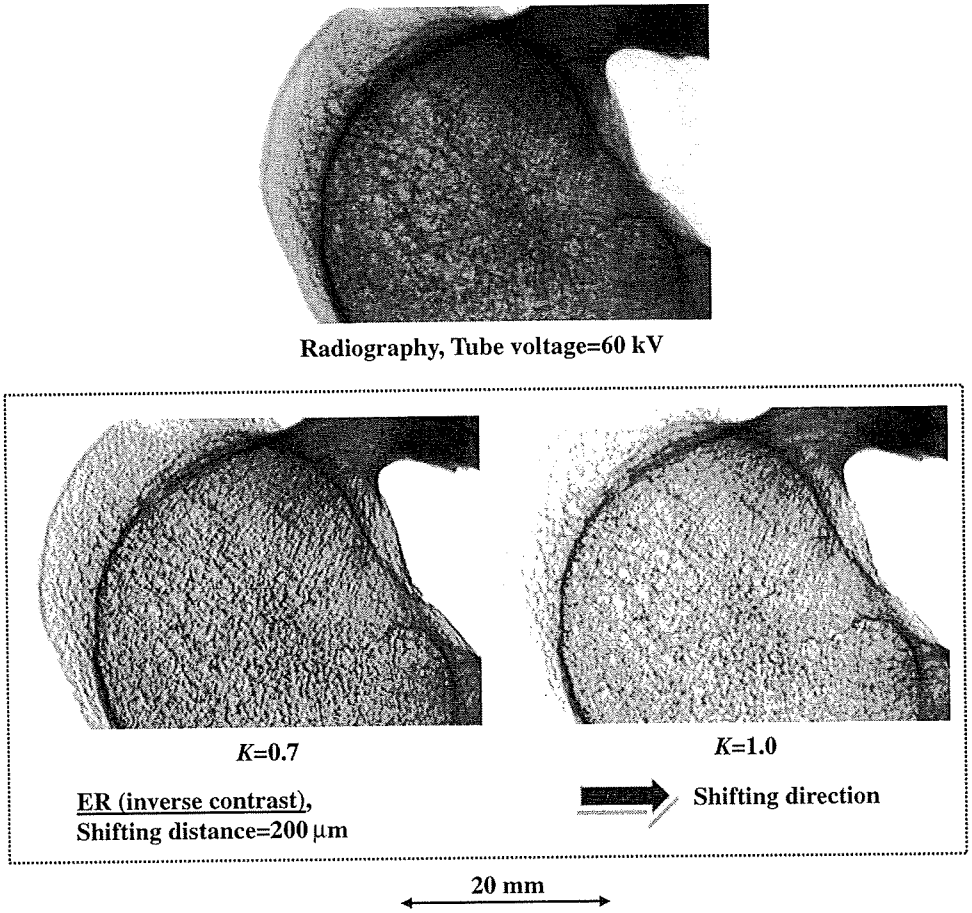

Fig. 11 Radiograms of a vertebra. With embossing, contrast resolution in the vertebra improves

To image a target region in vivo, we have to confine the X-ray spectra to optimal distributions for energy subtraction, and unnecessary regions for diagnosis should be deleted from radiograms. However, in cases where we carry out only embossment, single energy subtraction is usable. The tube voltage should be selected corresponding to radiographic objectives, and we have to use an optimal-element filter and to determine its effective thickness.

With this FPD, the exposure time was 5.0 s because the exposed dose rate from the 100-μm-focus tube was low owing to the maximum tube current of 0.5 mA. In addition, focal spot diameters below 1.0 mm are usable, and the exposure time decreases substantially with increasing spot diameter. Recently, a program for two-dimensional pixel shifting has been developed, and one-shot ER is realizable with single-energy subtraction.

Magnification radiography [19, 20] is useful for improving the spatial resolution in digital radiography. The spatial resolution improves with increasing magnification ratio, and the maximum ratio increases with decreasing focus diameter. Therefore, magnification ER utilizing energy subtraction can be performed, and a program for digital subtraction including a pixel-shifting function is useful for composing embossed images.

As compared with conventional radiography, the advantages of dual-energy ER are as follows: (1) contrast resolution can be increased up to approximately 1.0. (2) Edge-enhancement radiography such as phase-differential imaging is realizable. (3) Hard tissues are imaged effectively as compared with phase imaging. (4) Nano-particles and liquid contrast media in medical angiography can be observed as concavoconvex images with high contrast.

In human imaging, a computed radiography system is usable, and various applications will become possible as follows: angiography with iodine and gadolinium media, cancer diagnosis with nano-particles, hard-tissue (bone) imaging, and various radiographies with high contrast resolutions. In addition, an energy discriminating FPD system that can get spectral data is very useful for carrying out single-shot dual-energy subtraction with short exposure times.

This ER utilizing dual-energy subtraction is usable in various digital radiography systems, including a CR system. Therefore, we developed an ER program for CR utilizing a two-dimensional image-shifting function. However, it was difficult to carry out dual-energy ER precisely by using two imaging plates. We are currently developing a multi-slice mini-focus X-ray CT system

utilizing a 100-μm-focus tube, and embossed tomography with use of single- and dual-energy subtractions would be employed for increasing the contrast resolution of the target region. In our research, energy subtraction has been effective for imaging iodine contrast media and gadolinium oxide nano-particles, and ER is useful for edge enhancement radiography like phase imaging and for increasing the contrast resolution without a decrease in the spatial resolution.

Acknowledgments We would like to express our thanks to the reviewers for giving very helpful advice concerning our paper. This work was supported by Grants-in-Aid for Scientific Research and Advanced Medical Scientific Research from MECSST, Health and Labor Sciences Research Grants, Grants from the Keiryo Research Foundation, Promotion and Mutual Aid Corporation for Private Schools of Japan, the Japan Science and Technology Agency (JST), and the New Energy and Industrial Technology Development Organization (NEDO).

References

1. Thompson AC, Zeman HD, Brown GS, Morrison J, Reiser P, Padmanabahn V, et al. First operation of the medical research facility at the NSLS for coronary angiography. Rev Sci Instrum. 1992;63:625–8.
2. Mori H, Hyodo K, Tanaka E, Mohammed MU, Yamakawa A, Shinozaki Y, et al. Small-vessel radiography in situ with monochromatic synchrotoron radiation. Radiology. 1996;201:173–7.
3. Hyodo K, Ando M, Oku Y, Yamamoto S, Takeda T, Itai Y, et al. Development of a two-dimensional imaging system for clinical applications of intravenous coronary angiography using intense synchrotron radiation produced by a multipole wiggler. J Synchrotron Radiat. 1998;5:1123–6.
4. Momose A, Takeda T, Itai Y, Hirano K. Phase-contrast X-ray computed tomography for observing biological soft tissues. Nat Med. 1996;2:473–5.
5. Ando M, Maksimenko A, Sugiyama H, Pattanasiriwisawa W, Hyodo K, Uyama C. Simple X-ray dark- and bright-field imaging using achromatic Laue optics. Jpn J Appl Phys. 2002;41:L1016–8.
6. Ando M, Sugiyama H, Ichihara S, Endo T, Bando H, Yamasaki K, et al. Sharper image of breast cancer cells and stroma in dense breast using thinner angular filter under X-ray dark-field imaging. Jpn J Appl Phys. 2006;45:L740–3.
7. Iida S, Kawado S, Maehara T, Chikaura Y, Suzuki Y, Kajiwara K, et al. Plane-wave X-ray topography of grown-in microdefects in silicon crystals. J Phys D Appl Phys. 2005;38:A23–7.
8. Chen Y, Dhanaraj G, Dudley M, Sanchez EK, MacMillan MF. Sense determination of micropipes via grazing-incidence synchrotron white beam X-ray topography in 4H silicon carbide. Appl Phys Lett. 2007;91:071917.
9. Sato E, Sagae M, Tanaka E, Hayasi Y, Germer R, Mori H, et al. Quasi-monochromatic flash X-ray generator utilizing a disk-cathode molybdenum tube. Jpn J Appl Phys. 2004;43:7324–8.
10. Sato E, Tanaka E, Mori H, Kawai T, Sato S, Takayama K. Clean monochromatic X-ray irradiation from weakly ionized linear copper plasma. Opt Eng. 2005;44:049002–16.
11. Sato E, Hayasi Y, Germer R, Tanaka E, Mori H, Kawai T, et al. X-ray spectra from weakly ionized linear copper plasma. Jpn J Appl Phys. 2006;45:5301–6.
12. Sato E, Tanaka E, Mori H, Kawai T, Inoue T, Ogawa A, et al. Characteristic X-ray generator utilizing angle dependence of bremsstrahlung X-ray distribution. Jpn J Appl Phys. 2006;45:2845–9.
13. Sato E, Tanaka E, Mori H, Kawai T, Ichimaru T, Sato S, et al. Demonstration of enhanced K-edge angiography using a cerium target X-ray generator. Med Phys. 2004;31:3017–21.
14. Sato E, Tanaka E, Mori H, Kawai T, Inoue T, Ogawa A, et al. Variations in cerium X-ray spectra and enhanced K-edge angiography. Jpn J Appl Phys. 2005;44:8204–9.
15. Wilkins SW, Gureyev TE, Gao D, Pogany A, Stevenson AW. Phase-contrast imaging using polychromatic hard X-rays. Nature. 1996;384:335–8.
16. Bornefalk H, Lewin J, Danielsson M, Lundqvist M. Single-shot dual-energy subtraction mammography with electronic spectrum splitting: feasibility. Euro J Radiol. 2006;60:275–8.
17. Kido S, Kuriyama K, Hosomi N, Inoue E, Kuroda C, Horai T. Low-cost soft-copy display accuracy in the detection of pulmonary nodules by single-exposure dual-energy subtraction: comparison with hard-copy viewing. J Digit Imag. 2000;13:33–7.
18. Osawa A, Sato E, Matsukiyo H, Enomoto T, Watanabe M, Nagao J, et al. Novel embossed radiography system utilizing energy subtraction. Proc SPIE. 2008;7080:708003–16.
19. Ishisaka A, Ohara H, Honda C. A new method of analyzing edge effect in phase contrast imaging with incoherent X-rays. Opt Rev. 2000;7:566–72.
20. Enomoto T, Sato E, Sumiyama Y, Aizawa K, Watanabe M, Tanaka E, et al. Enhanced magnification angiography using 20-μm-focus tungsten tube. Jpn J Appl Phys. 2006;45:8005–9.

Mechanism of inhibition of tumor angiogenesis by β-hydroxyisovalerylshikonin

Yusuke Komi,[1,2] Yasuhiro Suzuki,[1,11] Mariko Shimamura,[3,12] Sachiko Kajimoto,[4] Shigeo Nakajo,[5] Michitaka Masuda,[6] Masabumi Shibuya,[7,13] Hiroyuki Itabe,[4] Kentaro Shimokado,[2] Peter Oettgen,[8] Kazuyasu Nakaya[9] and Soichi Kojima[1,10]

[1]Molecular Ligand Biology Research Team, Chemical Genomics Research Group, Chemical Biology Department, RIKEN Advanced Science Institute, 2-1 Hiroshima, Wako, Saitama 351-0198; [2]Vascular Medicine and Geriatrics, Tokyo Medical and Dental University Graduate School, 1-5-45 Yushima, Bunkyo, Tokyo 113-8519; [3]Medical R & D Center, Tokyo Metropolitan Institute of Medical Science, 3-18-22 Honkomagome, Bunkyo, Tokyo 113-8613; [4]Laboratory of Biological Chemistry, School of Pharmaceutical Sciences, Showa University, 1-5-8 Hatanodai, Shinagawa, Tokyo 142-8555; [5]Laboratory of Biochemistry, Yokohama College of Pharmacy, 601 Minato, Totsuka, Yokohama, Kanagawa 245-0066; [6]Department of Structural Analysis, National Cardiovascular Center Research Institute, 5-7-1 Fujishirodai, Suita, Osaka 565-8565; [7]Department of Genetics, Institute of Medical Science, University of Tokyo, 4-6-1 Shirokanedai, Minato, Tokyo 108-8639, Japan; [8]Division of Cardiology, Beth Israel Deaconess Medical Center, 330 Brookline Ave., Boston, MA 02115, USA; [9]Animal Cell Biological Engineering, Niigata University of Pharmacy and Applied Life Science, Niitsu, 265-1 Higashijima, Niigata 956-8603, Japan

(Received June 30, 2008/Revised October 20, 2008/Accepted October 31, 2008)

Shikonin and β-hydroxyisovalerylshikonin (β-HIVS) from *Lithospermum erythrorhizon* inhibit angiogenesis via inhibition of vascular endothelial growth factor receptors (VEGFR) in an adenosine triphosphate-non-competitive manner, although the underlying molecular mechanism has not been fully understood. In the present study, we found that β-HIVS inhibited angiogenesis within chicken chorioallantoic membrane approximately threefold more efficiently than shikonin. β-HIVS also significantly inhibited angiogenesis in two other assays, induced either by Lewis lung carcinoma cells implanted in mouse dorsal skin or by VEGF in s.c. implanted Matrigel plugs and metastasis of Lewis lung carcinoma cells to lung. Therefore, using β-HIVS as a bioprobe, we investigated the molecular mechanism of shikonin's anti-angiogenic actions. β-HIVS inhibited the phosphorylation and expression of VEGFR2 and Tie2 without affecting VEGFR1 and fibroblast growth factor receptor 1 levels. β-HIVS suppressed the phosphorylation but not the expression of extracellular signal-regulated kinase, and an Sp1-dependent transactivation of the *VEGFR2* and *Tie2* promoters, thereby suppressing the proliferation of vascular endothelial and progenitor cells. This was mimicked by an Sp1 inhibitor mithramycin A and partially rescued by Sp1 overexpression. These results implicate potential use of shikonin and β-HIVS as leading compounds for clinical application in the future by virtue of their unique properties including: (i) inhibition of VEGFR2 and Tie2 phosphorylation in an adenosine triphosphate-non-competitive manner; (ii) simultaneous inhibition of the phosphorylation and expression of VEGFR2 and Tie2; and (iii) bifunctional inhibition of the growth in endothelial cells and vascular remodeling. (*Cancer Sci* 2009; 100: 269–277)

Angiogenesis and/or vasculogenesis are essential for the growth of solid tumors.[1] Angiogenesis is the growth and sprouting of additional blood vessels from pre-existing blood vessels, while vasculogenesis is the formation of primitive vascular networks through differentiation of vascular progenitor cells (VPC) into endothelial cells.[1] Tumor cells produce angiogenic factors, such as vascular endothelial growth factor (VEGF) and angiopoietins (Ang)-1 and -2.[2,3] The VEGF/VEGF receptor (VEGFR) signaling pathway is essential for recruiting VPC and stimulating their differentiation into endothelial cells as well as for drawing endothelial cells from pre-existing blood vessels and stimulating their growth,[1] whereas the Ang/Tie2 signaling pathway is important for sustaining interaction between endothelial and mural cells and stabilizing the vasculature.[4] VEGF and Ang-1 bind to VEGFR and Tie2, respectively, on the surface of endothelial and progenitor cells, stimulate the activities of respective receptor tyrosine kinases and exert their biological functions.

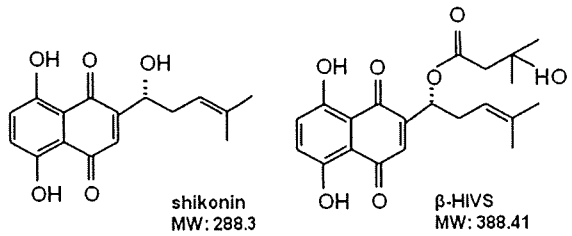

Fig. 1. Chemical structure of shikonin and β-hydroxyisovalerylshikonin (β-HIVS). MW, molecular weight.

Because newly formed blood vessels serve as a conduit for nutrition and a route for metastasis, tumor angiogenesis is a target for the treatment of solid tumors.[5] SU5416, ZD6474 and PTK787 have been developed as potent inhibitors of the phosphorylation of VEGFR tyrosine kinase.[6] A number of angiogenesis inhibitors have been developed to target receptor tyrosine kinases and/or their downstream mitogen activated protein kinase (MAPK) signaling cascades.[7]

Shikonin and β-hydroxyisovalerylshikonin (β-HIVS) are major components in the root (radix) of the plant *Lithospermum erythrorhizon*[8] (see Fig. 1 for their chemical structures), which is used traditionally as an oriental medicinal herb. They inhibit several receptor tyrosine kinases (e.g. v-Src, epidermal growth factor receptor and VEGFR) in an adenosine triphosphate (ATP)-non-competitive manner.[9] They also inhibit the growth of various lines of cancer cells and induce their apoptosis, suggesting their potential use as novel anticancer reagents.[9] Furthermore, Hisa *et al.*[10] reported that shikonin suppresses angiogenesis. However, the underlying molecular mechanism is not fully understood. Moreover, the direct effect of β-HIVS on the vascular endothelial cells and angiogenesis has not been studied.

In this manuscript, we aim to clarify the detailed molecular mechanism of anti-angiogenic activity of shikonins. First, based upon the previous report that β-HIVS inhibited tyrosine kinases

[10]To whom correspondence should be addressed.
E-mail: skojima@postman.riken.go.jp
[11]Present address: Department of Vascular Biology, Institute of Development, Aging and Cancer, Tohoku University, 4-1 Seiryo-machi, Aoba, Sendai, Miyagi 980-8575, Japan
[12]Present address: Tokyo Metropolitan Institute of Public Health, Tokyo Metropolitan Infectious Disease Surveillance Center, 3-24-1 Hyakunincho, Shinjuku, Tokyo 169-0073, Japan
[13]Present address: Department of Molecular Oncology, Tokyo Medical and Dental University Graduate School, 1-5-45 Yushima, Bunkyo, Tokyo 113-8519, Japan

doi: 10.1111/j.1349-7006.2008.01049.x
© 2008 Japanese Cancer Association

including VEGFR2 in endothelial cells stronger than shikonin, we explored the hypothesis that β-HIVS might inhibit angiogenesis stronger than shikonin and used β-HIVS to accomplish the aim. We found that β-HIVS suppressed the phosphorylation of both VEGFR2 and Tie2 as well as, surprisingly, the expression of both VEGFR2 and Tie2. This accompanied a reduction in an Sp1-dependent transactivation and upstream extracellular signal-regulated kinase (ERK) activation, culminating in reduced growth of vascular endothelial and progenitor cells, and inhibition of tumor angiogenesis. These results evidence that shikonin and β-HIVS have unique anti-angiogenic properties of bifunctional inhibition of the growth in endothelial cells and vascular remodeling and provide insights into development of novel anti-angiogenic inhibitors using shikonins as leading compounds in terms of: (i) simultaneous inhibition of the phosphorylation and expression of VEGFR2 and Tie2; and (ii) inhibition of VEGFR2 and Tie2 phosphorylation in an ATP-non-competitive manner.

Materials and Methods

Reagents. Shikonin was isolated from the plant, *Lithospermum radix*, as described before[8] and β-HIVS was purchased from Wako Pure Chemical Industries (Osaka, Japan). Mithramycin A was obtained from Sigma-Aldrich (St Louis, MO, USA). Sp1-expressing vector was constructed as described previously.[11]

Chicken chorioallantoic membrane (CAM) assay. Fertilized Dekalb chicken eggs (Omiya Kakin, Saitama, Japan) were placed in a humidified egg incubator. After a 4.5-day incubation at 38°C, a 1% solution of methylcellulose containing shikonin and β-HIVS at one of various concentrations was loaded inside a silicon ring that was placed onto the surface of the CAM. After further incubation for 2 days, a fat emulsion was injected into the chorioallantois, so that the vascular networks stood out against the white background of the lipid. Anti-angiogenic responses were evaluated under a stereomicroscope and photographed with a ×7.25 objective. Quantitative analyses were performed with angiogenesis-measuring software.[12]

Mouse dorsal air sac (DAS) assay. Millipore chambers (Millipore, Billerica, MA, USA) were filled with either RPMI-1640 medium alone or a suspension of 4×10^6 Lewis lung carcinoma (LLC) cells in the medium and sealed with membrane filters (0.45-μm pores). The chambers were implanted s.c. in DAS, created surgically by injection of an appropriate amount of air, in 7-week-old female ICR mice (Charles River, Yokohama, Japan). These mice were i.p. administered β-HIVS (30 mg/kg bodyweight) dissolved in a solution of 5% dimethylsulfoxide (DMSO), 15% Cremophor EL (Sigma-Aldrich) and 5% glucose in saline. One and three days later, the mice were killed with an overdose of diethyl ether. The skin was carefully removed and angiogenesis that had been induced around the chamber was examined under a stereomicroscope and photographed with a ×5.6 objective. Quantitative analyses were performed with angiogenesis-measuring software (ver. 2.0; KURABO, Osaka, Japan). All surgical procedures were performed under pentobarbital (Dainabot, Osaka, Japan) anesthesia. All animal experiments were performed according to the guidelines of the Animal Experiments Committee of RIKEN.

Matrigel plug assay. Matrigel (BD Biosciences, Bedford, MA, USA) was mixed with 200 units/mL heparin (Nacalai Tesque, Kyoto, Japan), with and without 50 ng/mL VEGF (Pepro Tech, Rocky Hill, NJ, USA) and 5 μM β-HIVS in 0.1% DMSO. The Matrigel mixture was injected s.c. into 5-week-old female C57BL/6 mice (Charles River). The mice were killed 7 days later. The Matrigel plugs were removed and fixed in 4% paraformaldehyde for 4 h, dehydrated through a graded ethanol series and embedded in paraffin (Nacalai Tesque). Vertical sections (5 μm) were mounted on slides and stained with hematoxylin–eosin or subjected to immunostaining as detailed below and observed under an inverted microscope (model DM IRB; Leica Microsystems, Wetzlar, Germany).

Table 1. Primers for reverse transcription polymerase chain reaction experiments

Gene		Sequence	Nucleotide#
Human	Sense	5′-TTTGGATGAGCAGTGTGAGC-3′	2415
VEGFR1	Antisense	5′-TTGGTTTCTTGCCTTGTTCC-3′	2866
Human	Sense	5′-GCATGGTCTTCTGTGAAGCA-3′	587
VEGFR2	Antisense	5′-CCAGAGATTCCATGCCACTT-3′	1018
Human	Sense	5′-TACACCTGCCTCATGCTCAG-3′	527
Tie2	Antisense	5′-GCAGAGACATCCTGGAAGC-3′	993
Human	Sense	5′-GGCAAGGAATTCAAACCTGAC-3′	697
FGFR1	Antisense	5′-CATCACGGCTGGTCTCTCTTC-3′	1224
Human	Sense	5′-ACCCAGAAGACTGTGGATGG-3′	610
GAPDH	Antisense	5′-CCCTGTTGCTGTAGCCAAAT-3′	1030
Human	Sense	5′-CTACCTCCACCATGCCAAGT-3′	48
VEGF	Antisense	5′-AAATGCTTTCTCCGCTCTGA-3′	458
Human	Sense	5′-TATGCCAGAACCCAAAAAGG-3′	855
Ang-1	Antisense	5′-GGGCACATTTGCACATACAG-3′	1258
Human	Sense	5′-CCACAAATGGCATCTACACG-3′	878
Ang-2	Antisense	5′-AAGTTGGAAGGACCACATGC-3′	1345

Metastasis assay. A suspension of 5×10^5 LLC cells was injected underneath the dorsal skin of 7-week-old female C57BL/6 mice. The mice were administered β-HIVS i.p. every other day for 3 weeks at a dose of 10 mg/kg bodyweight and killed with an overdose of diethyl ether. Lungs were carefully removed, examined under a microscope for the presence of tumors and photographed. Colonies of metastatic tumor cells observed on the whole lung surface were counted. No obvious adverse effects appeared after treatment of animals with β-HIVS under this condition.

Immunostaining. For fluorescence immunostaining, we used a combination of chicken antibodies against the cytoplasmic region of platelet/endothelial cell adhesion molecule-1 and fluorescein-5-isothiocyanate-conjugated rabbit antibodies against chicken IgG (Zymed Laboratories, Carlsbad, CA). Immunohistochemical staining of VEGFR2 was performed with an avidin–biotin kit (Vectastain Elite ABC kit; Vector Laboratories, Burlingame, CA, USA) according to the manufacturer's instructions using VEGFR2-specific rabbit monoclonal antibody (Cell Signaling Technology, Danvers, MA, USA). Immunostained sections were counterstained with Mayer's hematoxylin, dehydrated, mounted and observed under the inverted microscope.

Cell cultures. Culture of human umbilical vein endothelial cells (HUVEC) and maintenance, differentiation and sorting of the CCE/nLacZ ES cell cultures were performed as described, respectively.[12,13] VPC differentiated from CCE/nLacZ ES cell (the VEGFR2 [Flk-1] immunopositive cells) labeled with phycoerythrin were collected using the FACS VantageSE (Becton Dickinson Labware, Bedford, MA, USA) and recultured on dishes coated with type IV collagen in a modified minimum essential medium (Invitrogen, Carlsbad, CA, USA) supplemented with 10% fetal calf serum (Invitrogen). Bovine aortic endothelial cells (BAEC) were grown in a modified minimum essential medium containing 10% newborn calf serum (Hyclone Laboratories, Logan, UT, USA). NIH3T3 cells stably overexpressing VEGFR2 (NIH3T3-VEGFR2 cells) were maintained as described.[14]

Immunoprecipitation and western blotting analysis. Cells were washed several times with Tris-buffered saline (20 mM Tris-HCl, 137 mM NaCl) that contained Complete protease inhibitor cocktail (Roche, Indianapolis, IN, USA). Cells were lyzed in 1% Triton X-100 in 20 mM HEPES, pH 6.8 containing Complete protease inhibitor cocktail, 1 mM EDTA, 1 mM

doi: 10.1111/j.1349-7006.2008.01049.x
© 2008 Japanese Cancer Association

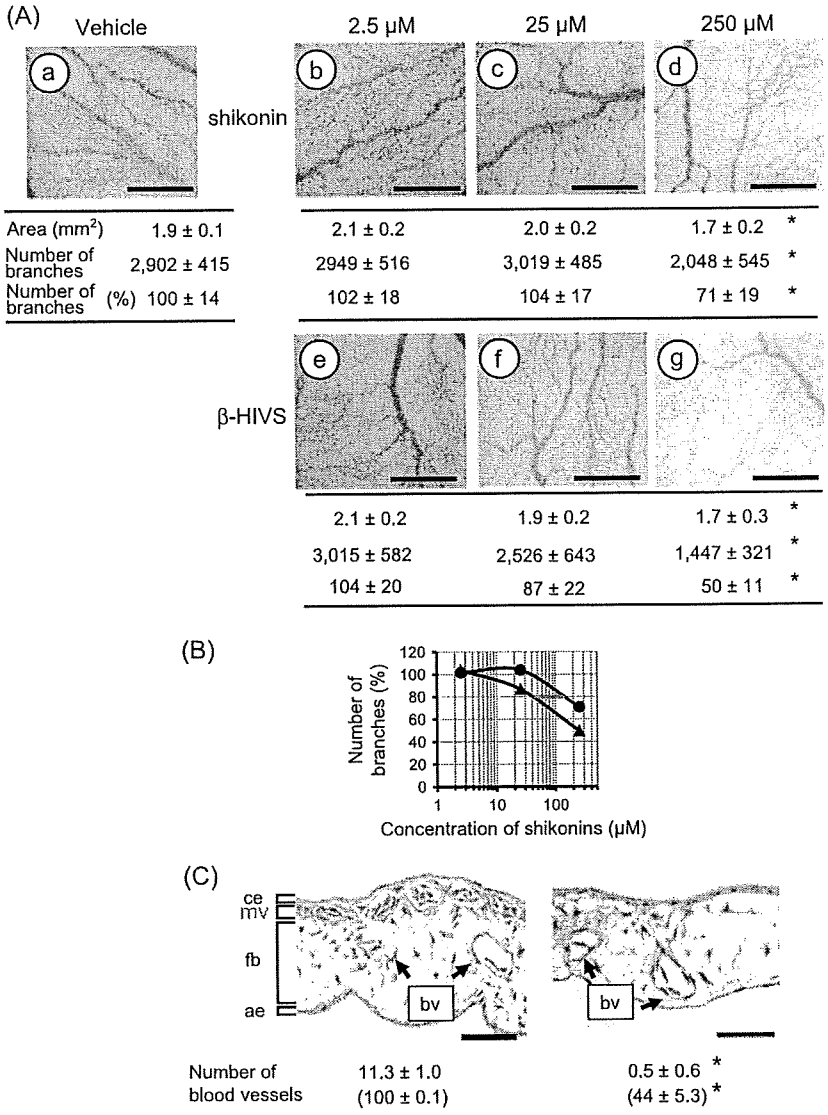

Fig. 2. Suppression of *in vivo* blood vessel formation and morphological changes induced in chicken chorioallantoic membrane (CAM) tissues by shikonins. (A) The 4.5-day-old CAM were treated with increasing concentrations of shikonin and β-hydroxyisovalerylshikonin (β-HIVS) for 48 h and then patterns of angiogenesis were photographed. (a) Vehicle (10% ethanol); (b) 2.5 μM shikonin; (c) 25 μM shikonin; (d) 250 μM shikonin; (e) 2.5 μM β-HIVS; (f) 25 μM β-HIVS; (g) 250 μM β-HIVS. Scale lines, 100 μm. The total area and the number of branches of blood vessels were analyzed with angiogenesis measuring software and are shown under each panel. Asterisks indicate significant differences ($P < 0.05$) from the control (a). A total of 18 eggs (six eggs/experiment × three experiments) were evaluated and representative results are shown. (B) Percentages of inhibition in the number of branches are plotted against concentrations of shikonin and β-HIVS. (●) Shikonin; (▲) β-HIVS. (C) The 4.5-day-old CAM were treated with vehicle (10% ethanol inside the ring = control). Note that the actual concentration of ethanol within CAM tissue was lower than that concentration due to diffusion of ethanol) (left panel) or 970 ng/egg β-HIVS (right panel) for 48 h. Vertical sections (3 μm) were mounted on slides, stained with hematoxylin–eosin, and observed under a Leica model DM IRB microscope (Leica Microsystems, Wetzlar, Germany). CAM tissue was composed of four different layers, including a thin chorionic epithelium (ce), microvasculatures (mv), a thick mesenchymal layer (fb) consisting of sparsely distributed fibroblasts and a few small blood vessels (bv), and a thin allantoic epithelium (ae). Scale lines, 50 μm. Representative micrographs from a total of 18 CAM tissues (six eggs/each × three experiments) are shown. Numbers of blood vessels were counted and are shown under each panel. Values are mean ± standard deviation ($n = 6$). Relative changes are shown as a percentage of control in parenthesis. Asterisks indicate significant differences ($P < 0.05$) from controls. (A–C) Representative results from two or three independent experiments that all gave similar results.

phenylmethylsulfonyl fluoride (PMSF) and 0.5 mM Na_3VO_5, and subjected to immunoprecipitation with anti-phosphotyrosine conjugated agarose beads (AG10; Upstate Biotechnology, Lake Placid, NY, USA) at 4°C overnight, washed with the lysis buffer three times and solubilized in sodium dodecylsulfate (SDS) buffer (200 mM Tris-HCl, pH 6.8, 6% w/v SDS, 30% glycerol, 150 mM dithiothreitol (DTT), 0.03% w/v Bromophenol Blue) followed by western analysis using Tie2-specific antibodies (1:1000 dilution, Upstate Biotechnology) or directly subjected to western analysis using phospho-VEGFR2-specific antibodies (1:1000 dilution; Cell Signaling Technology) or phospho-ERK-specific antibodies (1:2000 dilution, Cell Signaling Technology). Cell lysates were also subjected to western analysis using antibodies to VEGFR2, Tie2 and ERK, followed by reprobing with glyceraldehyde-3-phosphate dehydrogenase (GAPDH)-specific antibody (1:3000 dilution; HyTest, Turku, Finland) as a loading control. Immunoreactive bands of proteins were detected with ECL-Plus chemiluminescence reagents (GE Healthcare, Buckinghamshire, UK).

Reverse transcriptase-polymerase chain reaction (RT-PCR). Untreated (control cells) and cells treated with β-HIVS or mithramycin A were washed twice with phosphate-buffered saline and total RNA was extracted with an RNeasy Mini Kit (Qiagen, Valencia, CA, USA). RT-PCR was performed with the SuperScrip First-Strand Synthesis System (Invitrogen). Amplification by PCR was performed with pairs of specific primers summarized in Table 1.

Gel shift assay. Oligonucleotides corresponding to the GC box (Sp1 binding) motif within human VEGFR2 promoter (–85 to –64; 5′-CGGGAGAGACCCTCCTCCGCCC-3′)[15] were synthesized, double-stranded, end-labeled and used for the gel shift assays as described.[16] Nuclear proteins (6 μg) were incubated for 15 min at 4°C with 3.5 ng of ^{32}P-labeled probe in binding buffer (25 mM HEPES-KOH, 25 mM KCl, 5 mM $MgCl_2$, 50 μM $ZnSO_4$ and 8% glycerol) and separated on a 4% polyacrylamide gel at 4°C in running buffer (25 mM Tris-HCl, 190 mM glycine and 1 mM EDTA, pH 8.5). The gels were dried and radioactive bands were detected on a Fujix Bas 2500 Bio-imaging analyzer (Fuji Photo Film, Tokyo, Japan).

Transfection and luciferase assay. Transfections and assays of luciferase activity were performed as described previously[16]

© 2008 Japanese Cancer Association